CHAPTER 7

MONTE CARLO METHODS FOR SOLVING THE BOLTZMANN TRANSPORT EQUATION

Jean-Philippe M. Péraud, Colin D. Landon, & Nicolas G. Hadjiconstantinou*

Department of Mechanical Engineering, Massachusetts Institute of Technology, Cambridge, MA 02139, USA

*Address all correspondence to Nicolas G. Hadjiconstantinou E-mail: ngh@mit.edu

We review Monte Carlo methods for solving the Boltzmann equation for applications to small-scale transport processes, with particular emphasis on nanoscale heat transport as mediated by phonons. Our discussion reviews the numerical foundations of Monte Carlo algorithms, basic simulation methodology, as well as recent developments in the field. Examples of the latter include formulations for calculating the effective thermal conductivity of periodically nanostructured materials and variance-reduction methodologies for reducing the computational cost associated with statistical sampling of field properties of interest, such as the temperature and heat flux. Recent developments are presented in the context of applications of current practical interest, including multiscale problems that have motivated some of the most recent developments.

KEY WORDS: *Boltzmann equation, Monte Carlo, variance reduction, phonons, multiscale*

1. INTRODUCTION

1.1 Monte Carlo Methods

The term Monte Carlo (MC) is broadly used to refer to a wide class of computational methods that utilizes random sampling for obtaining numerical solutions. MC methods are ubiquitous in science and engineering; they are preferred due to their simplicity, but also because in many cases they lend themselves naturally to solution by simulation (as opposed to numerical discretization) thus tending to preserve an intuitive connection to the problem physics. Although MC methods are traditionally associated with and usually presented in the context of integration,[1] they find applications in a wide range of fields, such as atomistic modeling, solution of partial differential equations, optimization, and finance. They are particularly popular in statistical physics where high dimensionality makes approaches based on discretization inefficient and in many cases intractable; an example is the Metropolis algorithm[2] and its variants[3] used for simulating the various statistical mechanical ensembles.

In this review, we limit our discussion to stochastic particle methods for solving the Boltzmann transport equation. These methods are quite distinct from the Metropolis-type algorithms, which sample equilibrium distributions. Instead, the methods described here

ISSN: 1049–0787; ISBN: 1–978–56700–295–9/14/$35.00 + $00.00

NOMENCLATURE

A	macroscopic quantity of interest	f	single particle probability distribution function
$A_g(t)$	macroscopic quantity of interest corresponding to microscopic quantity g, at time t	f^{d}	distribution of deviations from a reference equilibrium
$\bar{A}$, $\bar{A}_g(t)$	estimate of macroscopic quantity from a sample of particles	$f^{\mathrm{eq}}(\omega, T)$ f_T^{eq}	Bose-Einstein distribution at temperature T
$\bar{A}_g(ss)$	steady-state estimate of A_g	f^{i}	initial distribution
$\mathcal{A}$	area	f^{loc}	local equilibrium distribution
C	specific heat per unit volume	f^{MB}	Maxwell-Boltzmann distribution
$C_{\omega,p}$	specific heat per unit volume per unit frequency (ω) as a function of ω and polarization p	$\mathbf{F}$	body force per unit mass
		F_i	cumulant distribution function in ith bin
C_A	computational particle population variance for calculating quantity A	$\mathbf{G}$	reciprocal lattice vector
		Γ	general coordinate in phase space, $(x, y, z, \omega, \theta, \phi, p, t)$
d	degree of specularity of a rough interface	$\hbar$	reduced Planck's constant $(= h/2\pi)$
$D(\omega, p)$	density of states	$\mathbf{k}$	phonon wave vector
$\delta(x-x_i)$, δ_{p,p_i}	dirac delta and Kronecker delta	k_{B}	Boltzmann's constant
		Kn	Knudsen number
e	energy distribution function $e = \hbar\omega f$	κ	thermal conductivity
		κ_{eff}	effective thermal conductivity
e^*	solution of the adjoint Boltzmann equation	L	characteristic length scale
		$\mathcal{L}$	linearized collision operator
e^{d}	distribution of energy deviations from a reference equilibrium	Λ	mean free path
		m	atomic mass
e_1^{in}, e_1^{out}, e_2^{in}, e_2^{out}	energy distribution entering or exiting a periodic cell through surfaces at $\mathbf{x}_1$ or $\mathbf{x}_2$	n	number density
		$\hat{\mathbf{n}}$	inward unit normal vector of the boundary of a surface or direction of a temperature gradient
$e_1^{\mathrm{d,in}}$, $e_1^{\mathrm{d,out}}$, $e_2^{\mathrm{d,in}}$, $e_2^{\mathrm{d,out}}$	deviational energy distribution entering or exiting a periodic cell through surfaces at $\mathbf{x}_1$ or $\mathbf{x}_2$	n_s	number of separate source terms
		N, $\dot{N}''$	number of phonons and number flux of phonons
e^{loc}	local equilibrium energy distribution	N^+, N^-	number of positive and negative particles
E_{tot}, $\dot{E}_{\mathrm{tot}}$	total deviational energy and its rate of change	N_{eff}	computational particle weight (the effective number of each particle)
$\mathrm{E}[X]$	expectation value of random variable X		
$\mathcal{E}_{\mathrm{eff}}^{\mathrm{d}}$	effective deviational energy (the amount of energy each deviational particle represents)	N_{part}	number of computational particles
		N_s	number of scattering events before termination of a particle in periodic and linearized problems
$\dot{\mathcal{E}}_{\mathrm{eff}}^{\mathrm{d}}$	effective deviational energy rate (the energy rate each deviational particle represents in a steady-state problem)	N_{source}	number of deviational particles emitted by a source term in a time step Δt

NOMENCLATURE (Continued)

ω, ω_i	phonon frequency and frequency of ith particle	t_i^{end}	exit or termination time of particle i
		t_i^{start}	emission time of particle i
$\omega_{0,i}$	central frequency of the ith spectral bin	t_{ss}	approximate time after which a system is considered at steady state
$\boldsymbol{\omega}$	vector of norm ω and direction (θ, ϕ)	T	temperature variable
		$\tilde{T}$	pseudo-temperature
$\boldsymbol{\Omega}$	solid angle	$\mathcal{T}_{12}$, $\mathcal{R}_{12}$	transmission and reflection coefficient between materials 1 and 2
p	phonon polarization index		
$P(\omega, p, T)$	probability of scattering event occurring		
$P_1(\theta)$, $P_2(\phi)$	probability density functions for polar and azimuthal angles	$\mathcal{T}$	time-averaging period
		τ	relaxation time
ψ_j	local density of energy absorption	θ, ϕ	polar and azimuthal angles
$\mathbf{q}''$, q_x''	heat flux, and x component of the heat flux	Θ_{D}, k_{D}, v_{D}	Debye temperature, wave vector, and velocity
Q_b, Q_s, Q_i	boundary, volumetric, and initial source terms in linearized formulation	$\mathbf{u}$	mean flow velocity
		U	energy density
		$U_{\text{cell}}^{\text{d}}$	deviational energy density in a cell
s_i	sign of the ith particle		
σ	differential collision cross section	$\mathbf{v}$	molecular velocity
		V	volume
$\sigma_{\bar{A}}$	statistical uncertainty in the estimate of quantity A	$\mathbf{V}_g$	group velocity
		$\mathbf{x}$, $\mathbf{x}_i$	spatial position vector and location of ith particle
t	time variable		
$\tilde{t}_1, ..., \tilde{t}_n$	measurement times in a transient linearized problem	Y	random variable representing the number of particles in a cell

generate stochastic realizations of a system evolving under the nonequilibrium, transient Boltzmann dynamics.

The intimate connection between MC methods and simulation may create the misconception that MC methods are modeling techniques. To the contrary, "proper" MC methods are rigorous numerical methods that can be shown to provide accurate solutions of the governing equation to which they are applied, provided appropriate choices are made for all numerical parameters (e.g., sufficiently small time step, sufficiently large number of particles), and the solution is correctly interpreted. Rigorous proofs that the methods discussed here reproduce the correct dynamics (under reasonable conditions) have been developed[4,5] in the case of the Boltzmann equation for gases, for which such methods have been known for a longer time.[6]

MC solutions are stochastic and need to be appropriately interpreted. This is usually achieved by sampling the solution field to obtain statistical estimates of its moments, which usually correspond to the macroscopic observables of interest (e.g., temperature). Although the associated statistical uncertainty can be reduced by increasing the number of samples,

this typically requires a proportional increase in the simulation time, while the magnitude of the uncertainty decreases with the square root of the number of independent samples.[1,7] This unfavorable scaling (for an M-fold reduction in statistical uncertainty, the simulation cost needs to increase by M^2) is, perhaps, the most important limitation associated with Monte Carlo methods; this limitation is a general feature of simulation methods which rely on statistical sampling for generating estimates of macroscopic observables.[7]

Overall, and for the reasons discussed later on in this chapter, when compared to deterministic methods for solving the Boltzmann transport equation (BTE), Monte Carlo methods are typically the method of choice, provided small-to-moderate statistical uncertainty (e.g., on the order of 0.1% or larger) is acceptable; if *significantly* smaller uncertainty is required (e.g., $<$0.01%), and depending on the problem, deterministic solution techniques may be preferable (provided a solution is at all possible).

1.2 Small-Scale Transport

Transport of mass, momentum, and energy can be modeled using conservation laws subject to "closures," which relate the microscopic fluxes of these quantities to the same. At the macroscopic scale, carrier motion is collision dominated and diffusive, leading to fluxes that are proportional to the gradients of the conserved quantities. This approach has been one of the bedrocks of engineering analysis at the macroscopic scale, because the resulting closed set of conservation laws, known as the Navier-Stokes-Fourier (NSF) set of equations, are robust, predictive, and not overly complex. As expected, this set of equations is valid as long as transport is diffusive, that is, as long as the characteristic length scale associated with transport is much larger than the carrier mean free path, the average distance traveled between scattering events with other carriers.

Deviation from diffusive transport is quantified by the Knudsen number

$$\mathrm{Kn} = \frac{\Lambda}{L}$$

where Λ denotes the mean free path and L the characteristic transport length scale. As expected, diffusive transport is valid for $\mathrm{Kn} \ll 1$; this regime is typically referred to as the continuum regime, although this terminology can be misleading:[8] in general, the range of validity of the diffusive transport approximation does not coincide with the range of validity of the continuum hypothesis because continuum conservation laws (with or without closures) can be written for regimes extending beyond $\mathrm{Kn} \ll 1$ (e.g., $\mathrm{Kn} > 0.1$).[9]

When the mean free path is much larger than the system length scale ($\mathrm{Kn} \gg 1$), carrier-carrier collisions are negligible and transport is ballistic. When the mean free path is on the same order as the system length scale ($0.1 \lesssim \mathrm{Kn} \lesssim 10$), transport exhibits a mixture of diffusive and ballistic behavior and is referred to as transitional.

Ballistic transport can be treated by neglecting carrier-carrier interactions, making it mathematically (analytically and numerically) significantly more tractable. Transitional transport is significantly more challenging to treat and typically requires modeling at the kinetic (or equivalent description) level; the governing equation for such kinetic descriptions, namely the Boltzmann equation, is discussed in Section 2.1.

Transitional transport has been extensively studied in gases,[10,11] which at standard temperature and pressure (STP) are sufficiently dilute to be modeled using kinetic theory. The molecular mean free path of air molecules at STP is $\sim$65 nm. Therefore, at macroscopic scales, transitional transport is important at low pressures, such as chemical vapor deposition processes,[12] in vacuum applications,[13] or in connection to the aerodynamics of space vehicles in the upper atmosphere,[10] from which the field of rarefied gas dynamics takes its name. More recent applications have concentrated on small-scale processes or phenomena. A notable example is the read-write head of a disk drive, which is suspended above the rotating disk at a distance that is comparable to the molecular mean free path of air. Correct description and design of the aerodynamics of this system requires modeling beyond the NSF equations.[14] Applications in the microelectromechanical domain include squeeze films,[15] Knudsen compressors,[16] and small-scale convective heat transfer.[17,18]

Another class of transport problems that has received considerable attention is heat transport in semiconductors. In these materials, heat is carried by lattice vibrations whose quantized unit is the phonon. With typical semiconductor feature sizes in the range of tens of nanometers to almost millimeters,[19] phonon transport can typically be treated semiclassically, using a Boltzmann equation. This approach is currently being used to calculate the thermal conductivity of bulk and nanostructured semiconductors,[20–29] to predict thermal transport behavior in small-scale and low-dimensional structures that are difficult to probe experimentally, such as graphene,[30–32] as well as to solve coupled electron-phonon transport problems.[33–38] New measurement techniques for probing the frequency-dependent response of phonon systems have also been aided by solution of the Boltzmann equation.[39–41]

After a brief introduction to kinetic theory and the Boltzmann equation, we will focus on Monte Carlo methods for obtaining solutions of the latter describing phonon transport. The chapter will focus on reviewing the basics of Monte Carlo simulation but also presenting exciting new developments that enable the treatment of problems of current practical interest.

2. BACKGROUND

2.1 Boltzmann Equation

The Boltzmann equation was introduced by Ludwig Boltzmann in 1872, as means of describing dilute gases at the kinetic level, but has found applications in a number of fields involving dilute carrier mediated transport.[27] It follows by considering conservation of particles in the phase space of molecular positions and velocities $(\mathbf{x}, \mathbf{v})$ and serves as an evolution equation for the single particle probability distribution function $f(t, \mathbf{x}, \mathbf{v})$, defined as the expected number of particles in a differential phase space element located at $(\mathbf{x}, \mathbf{v})$ at time t. It is usually expressed in the general form

$$\frac{\partial f}{\partial t} + \mathbf{v} \cdot \nabla_{\mathbf{x}} f + \mathbf{F} \cdot \nabla_{\mathbf{v}} f = \left[\frac{\partial f}{\partial t}\right]_{\text{coll}} \tag{1}$$

which serves to highlight its physical interpretation as a balance between collisionless advection [left-hand side (lhs)] and the effect of the collisions [right-hand side (rhs)]; the

latter is captured by the collision operator $[\partial f/\partial t]_{\text{coll}}$. Here, $\mathbf{F}$ represents the force per unit mass acting on the gas molecules.

For a gas of hard spheres, the collision operator takes the form[11]

$$\left[\frac{\partial f}{\partial t}\right]_{\text{coll}} = \int\int [f_1' f' - f_1\, f]\, ||\mathbf{v} - \mathbf{v}_1||\, \sigma\, d^2\mathbf{\Omega}\, d^3\mathbf{v}_1 \tag{2}$$

where $\sigma = \hat{d}^2/4$ is the differential collision cross-section for hard spheres, $\hat{d}$ is the gas molecule effective diameter, and $f' = f(t, \mathbf{x}, \mathbf{v}')$, $f_1 = f(t, \mathbf{x}, \mathbf{v}_1)$, $f_1' = f(t, \mathbf{x}, \mathbf{v}_1')$; here, $\{\mathbf{v}_1, \mathbf{v}\}$ are the pre collision velocities and $\{\mathbf{v}_1', \mathbf{v}'\}$ are the post collision velocities, related to the pre collision velocities through the scattering angle $\mathbf{\Omega}$. Integration in velocity space extends over all possible velocities, and the solid angle is integrated over the surface of the unit sphere.

The equilibrium solution of this equation is the Maxwell-Boltzmann distribution

$$f^{\text{MB}}(\mathbf{v}; n_{\text{MB}}, \mathbf{u}_{\text{MB}}, T_{\text{MB}}) = \frac{n_{\text{MB}}}{\pi^{3/2} v_{\text{MB}}^3} \exp\left(-\frac{||\mathbf{v} - \mathbf{u}_{\text{MB}}||^2}{v_{\text{MB}}^2}\right) \tag{3}$$

parameterized by the number density n_{MB}, flow velocity $\mathbf{u}_{\text{MB}}$ and temperature T_{MB}, reflecting the existence of three collisional invariants (mass, momentum, and energy). In Eq. (3), $v_{\text{MB}} = \sqrt{2k_{\text{B}}T_{\text{MB}}/m}$ is the most probable molecular speed, k_{B} is Boltzmann's constant, and m the molecular mass.

Physical quantities of interest can be recovered as moments of the distribution function. Specifically, the number density is given by

$$n(t, \mathbf{x}) = \int f(t, \mathbf{x}, \mathbf{v}) d^3\mathbf{v} \tag{4}$$

the gas flow velocity is given by

$$\mathbf{u}(t, \mathbf{x}) = \frac{1}{n} \int \mathbf{v} f(t, \mathbf{x}, \mathbf{v}) d^3\mathbf{v} \tag{5}$$

and the temperature is given by

$$T(t, \mathbf{x}) = \frac{m}{3nk_{\text{B}}} \int ||\mathbf{v} - \mathbf{u}_{\text{MB}}||^2\, f\, d^3\mathbf{v} \tag{6}$$

2.2 Boltzmann Equation for Phonon Transport

As introduced above, the principal carriers of thermal energy in insulating solids are lattice vibrations, whose quantized representation is the phonon. This quantum mechanical description incorporates both particle- and wavelike phenomena, while the Boltzmann equation is applicable only to distributions of classical particles. Fortunately, for silicon devices (taken here as typical) with length scales above 10–30 nm, coherence effects can be neglected and phonon distributions can be treated as a system of dilute classical particles or a "phonon gas."[27,42–44] The corresponding evolution equation is a Boltzmann-type transport equation of the form

$$\frac{\partial f}{\partial t} + \nabla_{\mathbf{k}}\omega(\mathbf{k}, p) \cdot \nabla_{\mathbf{x}} f = \left[\frac{\partial f}{\partial t}\right]_{\text{coll}} \tag{7}$$

written in the phase space of phonon positions and wave vectors $(\mathbf{x}, \mathbf{k})$ and neglecting the body force term, which is of limited interest in the present context. The wavelike nature of the phonons must still be considered in order to relate phonon momentum $\hbar\mathbf{k}$ and energy $\hbar\omega$, where phonon frequency ω is a function of the wave vector, $\mathbf{k}$, through the dispersion relation $\omega(\mathbf{k}, p)$; here, p denotes the polarization. Our discussion will proceed in the context of three-dimensional materials; applications to two-dimensional materials, such as graphene,[45] directly follow as extensions. Discussion on applications of Monte Carlo methods to transport in graphene can be found in Refs. 46–48.

A principal difference between a molecular and a phonon gas is the nature of scattering events. In the case of phonons, phonon number and momentum need not be conserved during interactions. A "two-phonon" scattering process occurs when a single phonon is scattered into a new state by an impurity; this results in a change in the phonon momentum ($\mathbf{k} \neq \mathbf{k}'$), but conserves energy ($\hbar\omega = \hbar\omega'$). Three-phonon scattering occurs when two phonons combine to create a third phonon (type I processes) or a single phonon decays into two phonons (type II processes). The conservation requirements for three-phonon scattering can be expressed as

$$\mathbf{k} \pm \mathbf{k}' = \mathbf{k}'' + \mathbf{H} \quad (\text{type I/II processes}), \tag{8}$$

and

$$\omega \pm \omega' = \omega'' \quad (\text{type I/II processes}), \tag{9}$$

In the above, for umklapp processes $\mathbf{H} = \mathbf{G}$, where $\mathbf{G}$ is the reciprocal lattice vector, while for normal processes $\mathbf{H} = \mathbf{0}$. Umklapp scattering does not conserve momentum ($\mathbf{G} \neq 0$) and hence is the primary contributor to the thermal resistivity of a pure semiconductor. Four-phonon and higher order processes are typically negligible.[49]

Considering only two- and three-phonon scattering events and scattering into as well as out of a state, the scattering operator can be written as follows:[50,51]

$$\begin{aligned}\left[\frac{\partial f}{\partial t}\right]_{\text{coll}} &= \sum_{\mathbf{k}',p'} \left\{f_{\mathbf{k}'p'}(f_{\mathbf{k}p}+1) - f_{\mathbf{k}p}(f_{\mathbf{k}'p'}+1)\right\}\mathcal{Q}_{\mathbf{k}p}^{\mathbf{k}'p'} \\ &+ \sum_{\mathbf{k}'p',\mathbf{k}''p''} \left\{(f_{\mathbf{k}p}+1)(f_{\mathbf{k}'p'}+1)f_{\mathbf{k}''p''} - f_{\mathbf{k}p}f_{\mathbf{k}'p'}(f_{\mathbf{k}''p''}+1)\right\}\mathcal{Q}_{\mathbf{k}p,\mathbf{k}'p'}^{\mathbf{k}''p''} \\ &+ \frac{1}{2}\sum_{\mathbf{k}'p',\mathbf{k}''p''} \left\{(f_{\mathbf{k}p}+1)f_{\mathbf{k}'p'}f_{\mathbf{k}''p''} - f_{\mathbf{k}p}(f_{\mathbf{k}'p'}+1)(f_{\mathbf{k}''p''}+1)\right\}\mathcal{Q}_{\mathbf{k}p}^{\mathbf{k}'p',\mathbf{k}''p''}\end{aligned} \tag{10}$$

where $\mathcal{Q}$ is the transition probability matrix as dictated by the Hamiltonian of interaction and the appropriate conservation laws.[51]

Physical observables can be calculated by summing the contributions of all phonons in the region of interest over reciprocal space. For isotropic systems with closely spaced energy levels (i.e., of relatively large size), the summation may be converted to an integration over frequency using the density of states, which for three-dimensional materials has the form

$$D(\omega, p) = \frac{k(\omega, p)^2}{2\pi^2 V_g(\omega, p)} \tag{11}$$

where $V_g(\omega, p) \equiv \|\nabla_{\mathbf{k}}\omega(\mathbf{k}, p)\|$ is the group velocity. Using this approach, the number of phonons per unit volume is given by

$$n(t, \mathbf{x}) = \sum_p \int\int\int f(t, \mathbf{x}, \omega, \theta, \phi, p) \frac{D(\omega, p)}{4\pi} \sin(\theta) d\omega d\theta d\phi \tag{12}$$

where θ and ϕ respectively refer to the polar and azimuthal angle in a system of spherical coordinates. To simplify the notation, we use $(\boldsymbol{\omega})$ to denote the vector whose norm is ω and whose direction is given by θ and ϕ, and represent the integration over these three components with a simple integral sign. The differential $\sin(\theta)d\omega d\theta d\phi$ is then denoted by $d^3\boldsymbol{\omega}$. Using this notation, the energy per unit volume is given by

$$U(t, \mathbf{x}) = \sum_p \int \hbar\omega f(t, \mathbf{x}, \boldsymbol{\omega}, p) \frac{D(\omega, p)}{4\pi} d^3\boldsymbol{\omega} \tag{13}$$

and the heat flux is given by

$$\mathbf{q}''(t, \mathbf{x}) = \sum_p \int \hbar\omega \mathbf{V}_g f(t, \mathbf{x}, \boldsymbol{\omega}, p) \frac{D(\omega, p)}{4\pi} d^3\boldsymbol{\omega} \tag{14}$$

The equilibrium distribution is given by the Bose-Einstein expression

$$f^{\text{eq}}(\omega, T_{\text{eq}}) = \frac{1}{\exp\left(\hbar\omega / k_{\text{B}} T_{\text{eq}}\right) - 1} \tag{15}$$

which is parameterized only by the temperature, reflecting the presence of only one "collisional invariant," namely, the energy. In systems out of equilibrium, the local temperature can be defined in terms of an equilibrium distribution with the same energy density, by solving

$$\sum_p \int \hbar\omega f(t, \mathbf{x}, \boldsymbol{\omega}, p) \frac{D(\omega, p)}{4\pi} d^3\boldsymbol{\omega} = \sum_p \int \hbar\omega f^{\text{eq}}(\omega, T) D(\omega, p) d\omega \tag{16}$$

for $T = T(t, \mathbf{x})$.

Comprehensive reviews of phonon physics and the phonon BTE can be found in numerous sources (e.g., Refs. 27, 50, and 52–54). The readers are referred to these sources for more information.

2.3 Relaxation-Time Approximation

The complexity associated with the Boltzmann equation is due, in large part, to the structure of the collision operator. For example, in the hard-sphere case, the collision operator

makes the Boltzmann equation nonlinear and integrodifferential. This complexity can be mitigated by replacing the collision operator with a model that is significantly simpler.

Perhaps the most popular approach amounts to assuming that the role of carrier-carrier interactions is to drive the system toward the local equilibrium, characterized by f^{loc}, an equilibrium distribution corresponding to the system local properties (for τ = const). The resulting model,

$$\left[\frac{\partial f}{\partial t}\right]_{\text{coll}} = -\frac{f - f^{\text{loc}}}{\tau} \tag{17}$$

is known in general as the relaxation time-approximation.[11,52]

In the rarefied gas dynamics literature, this model is known as the Bhatnagar-Gross-Krook model[55]. Although the relaxation-time formulation is approximate* and neglects the details of the relaxation pathways, it has been very successful due to its simplicity, but also because, by construction, it satisfies a minimal set of fundamental requirements, such as preserving the correct equilibrium distribution and conservation laws, as well as satisfying the H-theorem (see Ref. 56 for the dilute-gas case).

The relaxation time model has also found widespread use in the electron, phonon, and neutron literature. In the case of the phonon Boltzmann equation,[57,58] in order to capture some of the complexity of phonon-phonon interactions, the relaxation time is usually taken to depend on the carrier state [e.g., $\tau = \tau(\omega, p, T)$]. In this case, the parameters of f^{loc} do not take their local values.[11,28] This is further discussed in Section 3.3.

The limitations of the relaxation-time approximation for phonon transport will be briefly discussed in Section 3.8 in the context of phonon Monte Carlo simulations.

2.4 Validity of Fourier's Law

One of the greatest successes of kinetic theory is the celebrated Chapman-Enskog (CE) solution of the Boltzmann equation,[11,59] which shows how the NSF set of equations arises asymptotically from the Boltzmann equation in the limit $\text{Kn} \ll 1$. Although this procedure was originally performed for the hard-sphere operator (for an outline see Ref. 9, while more details can be found in Ref. 59) and subsequently for a variety of collision operators, it can be most easily demonstrated using the simple relaxation-time model discussed above.

In what follows, we will outline the CE solution procedure for the simple case of a steady, one-dimensional phonon-transport problem in the relaxation-time approximation. For simplicity, here we consider the Debye model coupled with the gray medium approximation, which leads to the following definition $\text{Kn} = V_g\tau/L$ for the Knudsen number. Our objective here is to highlight a common misconception on the validity of Fourier's law

$$\mathbf{q}'' = -\kappa\nabla_{\mathbf{x}}T \tag{18}$$

and the associated kinetic-theory expression for κ.

For the system considered here, the Boltzmann equation reduces to

*In the dilute gas case, it is well known[11] that it leads to the wrong Prandtl number, namely 1, instead of $2/3$.

$$V_g \cos(\theta)\frac{\partial f}{\partial x} = \frac{f^{\text{loc}} - f}{\tau} \tag{19}$$

where, without loss of generality, we have assumed variations to take place in the x direction and θ is the polar angle with respect to this direction. The CE solution procedure amounts to postulating a series solution of the form

$$f = f^{\text{loc}} + \text{Kn}\, h_1 + \text{Kn}^2 h_2 + O(\text{Kn}^3) \tag{20}$$

in which h_1 and h_2 correspond to higher order corrections from the local equilibrium. The form of this expansion is motivated by the physical observation that $f \to f^{\text{loc}}$ as $\text{Kn} \to 0$, which mathematically can be seen by rewriting (19) as follows:

$$\cos(\theta)\frac{\partial f}{\partial x^*} = \frac{f^{\text{loc}} - f}{\text{Kn}} \tag{21}$$

where $x^* = x/L$. Substituting (20) into *both sides of* (21) and equating equal powers of Kn allows one to easily solve for h_1, yielding the following well-known expression for the distribution function:

$$f = f^{\text{loc}} - V_g \tau \cos(\theta)\frac{df^{\text{loc}}}{dx} + \mathcal{O}(\text{Kn}^2) \tag{22}$$

Inserting (22) into Eq. (14), we arrive at the following relation for the x component of the heat flux:

$$q_x'' = -\left[\frac{1}{2}\sum_p \int\int \tau V_g^2 C_{\omega,p} d\omega \cos^2(\theta)\sin(\theta) d\theta\right]\frac{dT}{dx} + \text{Kn}^2 \sum_p \int\int \hbar\omega V_g h_2 \frac{D(\omega,p)}{2} d\omega \cos(\theta)\sin(\theta) d\theta + \mathcal{O}(\text{Kn}^3) \tag{23}$$

where $C_{\omega,p}$ refers to the specific heat per frequency per unit volume $\hbar\omega D(\omega,p) df^{\text{loc}}/dT$ with

$$\frac{df^{\text{loc}}}{dT} = \frac{\hbar\omega}{k_{\text{B}} T_{\text{loc}}^2} \frac{1}{4\sinh^2(\hbar\omega/2k_{\text{B}}T_{\text{loc}})} \tag{24}$$

In Eq. (23), the term involving h_2 is explicitly retained to highlight the fact that the familiar Fourier law (18) and the associated expression for the thermal conductivity

$$\kappa = -\frac{q_x''}{dT/dx} = \frac{1}{3}\sum_p \int \tau V_g^2 C_{\omega,p} d\omega \tag{25}$$

follow from the above only if $\text{Kn} \ll 1$, whereby terms of order Kn^2 and higher are negligible.

In other words, use of Eqs. (18) and (25) for $\text{Kn} \gtrsim 0.1$ is not justified; as shown by (23), if Kn is no longer small, with the exception of a small number of special cases (e.g.,

the thin-film problem[60,61]) the heat flux is not necessarily proportional to the temperature gradient and thus the concept of thermal conductivity [as defined by (25)] no longer holds.

This can be further illustrated using the following example: consider the heat transfer in the material just studied, in the case that is enclosed between two boundaries that are sufficiently close that Kn $\gg 1$, and held at temperatures $T_0 \pm \Delta T/2$, with $\Delta T \ll T_0$. In this ballistic limit, the heat flux across this slab of material can be readily shown[62] to equal

$$\begin{aligned} q_x'' &= -k_{\mathrm{B}} \sum_p \int \left[\frac{\hbar\omega}{2k_{\mathrm{B}}T_0 \sinh\left(\hbar\omega/2k_{\mathrm{B}}T_0\right)} \right]^2 \frac{V_g D}{4} d\omega \Delta T \\ &= -\sum_p \int \frac{C_{\omega,p} V_g}{4} d\omega \Delta T \end{aligned} \tag{26}$$

From this expression, it is clear that for $Kn \gg 1$, $q_x'' \neq -\kappa(dT/dx)$; in fact, q_x'' is proportional to the temperature difference between the two boundaries but not the temperature gradient. Insisting on the definition $\kappa = -q_x''/(dT/dx)$ or even $\kappa = -q_x'' L/\Delta T$ leads to a contradiction because it results in a material property that is geometry dependent. This should come as no surprise because, as argued above, no theoretical basis exists for using Fourier's law to calculate thermal conductivities in the transition and ballistic regimes.

Despite the above evidence to the contrary, the misconception that the thermal conductivity for Kn $\gtrsim 0.1$ can be calculated using Fourier's law with τ interpreted as the average time between scattering events including the effect of boundaries is still popular. To disprove this, consider the following:

- From the development of Eqs. (19)–(25), it follows that τ in (25) is the material intrinsic scattering rate with no consideration to boundaries.
- Substitution of $\tau = L/V_g$ in (25) yields[62]

$$q_x'' = -\sum_p \int \frac{C_{\omega,p} V_g}{3} d\omega \Delta T, \tag{27}$$

  while substituting the "more correct" $\tau = L/V_g|\cos(\theta)|$ in the first term of (23) and then performing the θ-integration yields

$$q_x'' = -\sum_p \int \frac{C_{\omega,p} V_g}{2} d\omega \Delta T \tag{28}$$

  Neither of these expressions matches the ballistic value (26).

Another example where using Fourier's law for Kn > 0.1 yields incorrect results is given in Section 6.6.1. This is again because, other than dimensional arguments, no theoretical basis for using Fourier's law for Kn > 0.1 exists.

The inability of the thermal conductivity to describe material behavior in the presence of ballistic effects is a manifestation of the fact that the diffusive and ballistic transport

modes are fundamentally different. On the other hand, the desire for a unified measure of material performance that is valid for all Kn has led to the use of the concept of the "*effective* thermal conductivity"

$$\kappa_{\text{eff}} = \frac{-q''_x L}{\Delta T} \tag{29}$$

Clearly, this quantity has the units of thermal conductivity and reduces to the latter in the limit Kn $\to 0$, whereas for Kn > 0 it serves as a convenient way of comparing the thermal conductance of different systems (in convenient and familiar units).

However, it should also be clear that this property does not extend Fourier's law to the Kn > 0.1 regime. This can be easily verified by considering the ballistic (and linearized) problem discussed above. Using Eqs. (26), (25), and (29), we conclude that for Kn $\to \infty$, $\kappa_{\text{eff}} = 3\kappa/4$. Using this value in Fourier's law leads to the prediction that the temperature profile for Kn $\to \infty$ will be linear between the two boundary values $T_0 + \Delta T/2$ and $T_0 - \Delta T/2$, which is incorrect: the temperature profile for Kn $\to \infty$, is in fact constant at T_0 (let $t \to \infty$ in Eq. (B5) in Ref. 61; the profile for Kn $= 10$, also suitable for illustrating this, can be found in Fig. 1).

In other words, although κ_{eff} can be useful, as is used in this chapter, for comparing the relative performance of various systems by comparing their relative overall thermal conductance, it is not a material property; it depends on the system material, as well as length scale and geometry, and cannot be used in Fourier's law to solve for the temperature field. In fact, because it is geometry dependent, it cannot even be used to calculate the heat flux (on which it was "trained") for the same material in a different geometry.

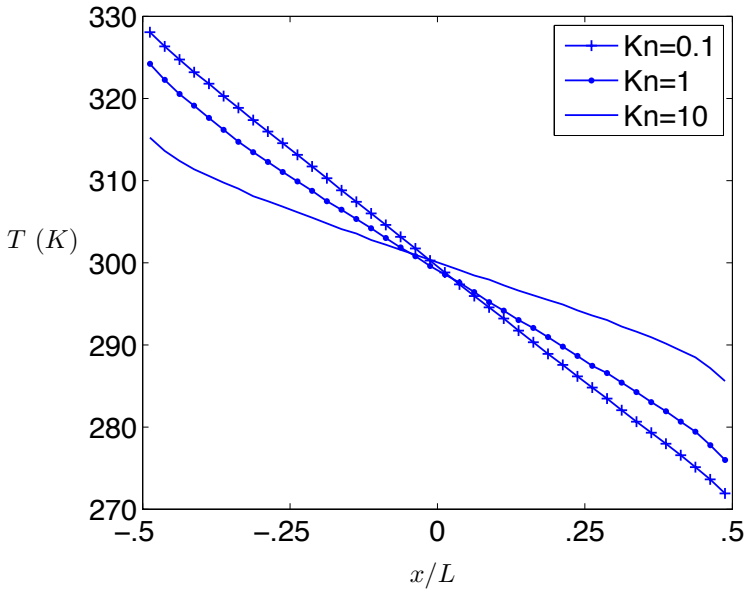

FIG. 1: Steady state temperature profile in a one-dimensional silicon system with boundaries at temperatures $T_l = 330$ K and $T_r = 270$ K at different Knudsen numbers. More details can be found in Section 4.3.

2.5 Distinction between Local and Global Equilibrium

In contrast to the aerodynamics of atmospheric reentry vehicles extensively studied in the rarefied gas dynamics literature,[10] nanoscale applications are typically characterized by low-speed flows and small temperature differences,[8,63] which in the context of MC simulation correspond to low signals. In rarefied gas dynamics, the difference between low- and high-signal phenomena can be quantified by the Mach number or the ratio $\Delta T/T_0$, where ΔT is the characteristic temperature change in the domain and T_0 a reference temperature. In high-signal problems $(\mathrm{Ma},\ \Delta T/T_0) \gtrsim 1$, while in nanoscale phenomena, typically $(\mathrm{Ma}, \Delta T/T_0) \ll 1$. The latter ($\Delta T/T_0 \ll 1$) is also typically valid for nanoscale phonon transport,[61,64] and implies[65] that the deviation from the reference equilibrium distribution $f^{\mathrm{eq}}(\omega, T_0)$ is small. When this condition is satisfied, the BTE may be linearized, resulting in a description which is valid for small $\Delta T/T_0$, but all Kn.

The objective of this section is to emphasize the latter point, namely, that a small deviation from a reference equilibrium ($\Delta T/T_0 \ll 1$) is not equivalent to and does not imply diffusive transport (Fourier behavior, Kn $\ll 1$). This can be seen from the fact that $\Delta T/T_0 \ll 1$ constrains the energy density associated with the distribution function (to be close to that of an equilibrium distribution at T_0) but does not require collisions to be dominant over advection. This is also evident from the fact that the requirement $\Delta T/T_0 \ll 1$ does not involve a length scale restriction and can thus be satisfied for arbitrary length scales (Kn).

2.6 Direct Simulation Monte Carlo

The methods on which this chapter focuses originate from Bird's direct simulation Monte Carlo (DSMC) method, introduced in his seminal 1963 paper.[6] DSMC is now the method of choice for solving the Boltzmann equation in the field of rarefied gas dynamics due to a number of factors: first, the high dimensionality associated with $f(t, \mathbf{x}, \mathbf{v})$ makes numerical methods based on discretization computationally expensive, both in terms of CPU time and storage; second, the particle formulation employed by DSMC is ideal for accurately and *stably* capturing the propagation of traveling discontinuities in the distribution function[66] resulting from the advection operator in the Boltzmann equation [lhs in Eq. (1)]; finally, the DSMC algorithm combines simplicity with an intuitive formulation that naturally employs importance sampling for improved computational efficiency.[67]

DSMC solves[4] the Boltzmann equation using discretization in time; each time step of length Δt is split into a collisionless advection and a collision substep.[10] Numerically, this corresponds to a splitting scheme[68] in which the collisionless advection substep integrates

$$\frac{\partial f}{\partial t} + \mathbf{v} \cdot \nabla_{\mathbf{x}} f + \mathbf{F} \cdot \nabla_{\mathbf{v}} f = 0 \tag{30}$$

while the collision substep integrates

$$\frac{\partial f}{\partial t} = \left[\frac{\partial f}{\partial t}\right]_{\mathrm{coll}} \tag{31}$$

During the advection substep, particles move ballistically (according to their velocities and accelerations). During the collision substep, the distribution function is updated by processing binary collisions between collision pairs chosen from within the same computational cell of linear size Δx, using an acceptance-rejection procedure.[69] This introduces the second important mode of discretization in this algorithm, as it corresponds to treating the distribution function as spatially homogeneous within each cell. Detailed descriptions of the DSMC algorithm can be found in Refs. 69 and 70.

This algorithm has been shown[4] to converge to solutions of the Boltzmann equation, provided that a sufficiently large number of particles is used and the integration time step and cell size are appropriately small ($\Delta t \ll \Lambda/\sqrt{2k_{\mathrm{B}}T_0/m}$ and $\Delta x \ll \Lambda$ with T_0 an appropriate reference temperature). By analyzing the time-splitting procedure using Green-Kubo theory, it has been shown that *transport coefficients* are predicted correctly to second order in the time step, provided the splitting is appropriately symmetrized.[71] It has also been shown that transport coefficients are predicted correctly to second-order accuracy in the cell size.[70] Perhaps surprisingly, the above results[70,71] provide not only the convergence rate, but also the proportionality constant; they predict errors on the order of 5–10% for cell sizes on the order of one mean free path and time steps on the order of one mean free time ($\Lambda/\sqrt{2k_{\mathrm{B}}T_0/m}$). These theoretical predictions have been extensively validated.[70–74] Rader et al.[74] have also empirically shown that the error in the transport coefficients due to a finite number of particles is proportional to $1/N_{\mathrm{part}}$, thus validating conventional wisdom that reasonably accurate computations could be achieved with as little as 20 particles per cell, but also that for highly accurate simulations more than 100 particles per cell are required.[75]

Hydrodynamic properties calculated by DSMC also suffer from statistical uncertainty due to finite sampling; according to the central limit theorem, the uncertainty is inversely proportional to the square root of the number of *independent* samples. Hadjiconstantinou et al.[7] showed that explicit expressions for the statistical uncertainty can be developed for all physical properties of interest using statistical mechanics to calculate the population variance associated with each property. The use of equilibrium statistical mechanics is justified when characteristic temperature changes are small (e.g., compared to the absolute reference temperature) as is typical in microscale applications.[8] These results were validated by DSMC and molecular dynamics simulations in Ref. 7. A theoretical description for fluctuations for phonon MC simulations is presented in Section 3.5. MC methods for solving the BTE for phonon transport are discussed in Section 3.

3. MONTE CARLO SOLUTION OF THE PHONON BTE

In 1988, in order to interpret interesting results from thermal conductance experiments at low temperature, Klitsner et al. developed the first phonon Monte Carlo, albeit without considering internal scattering mechanisms that were irrelevant due to the long phonon mean free path at low temperature.[20] In 1994, Peterson[76] developed a Monte Carlo simulation that included phonon-phonon scattering using the relaxation-time approximation. Since that time, a number of important advancements have been introduced, including dispersion relation improvements,[77,78] frequency-dependent relaxation times,[77] scattering

substep energy conservation,[79] periodic boundary conditions,[24,28] and variance-reduced formulations.[61,64] Section 3.1 describes the state of the art for the traditional formulation of phonon Monte Carlo, which is a direct extension of the DSMC method discussed in Section 2.6.

The principal aim of the phonon Monte Carlo method is to generate samples of the distribution function, typically to be used for evaluating Eqs. (13) and (14). This is achieved by approximating the distribution function using N_{part} computational particles

$$f(t, \mathbf{x}, \boldsymbol{\omega}, p)\frac{D(\omega, p)}{4\pi} \approx N_{\text{eff}} \sum_{i=1}^{N_{\text{part}}} \delta^3(\mathbf{x} - \mathbf{x}_i(t))\delta^3(\boldsymbol{\omega} - \boldsymbol{\omega}_i(t))\delta_{p,p_i(t)} \tag{32}$$

where N_{eff} is the effective number of phonons characterized by the (same) properties $[\mathbf{x}_i(t), \boldsymbol{\omega}_i(t), p_i(t)]$ represented by the computational particle i.[35,77] The concept of the effective number is used because, typically, the number of real phonons per unit volume is too large to directly simulate. Using the Debye model as an example, the number density of phonons in silicon (Debye temperature of 645 K, coordination number of 8 and a lattice parameter of 5.4307 Å) at 300 K is 5×10^{28} phonons per cubic meter. In other words, a cubic cell with side 10 nm contains $\sim 5 \times 10^4$ phonons. Although in some cases it may be possible to simulate this number of particles in each computational cell, in general, a smaller number is sufficient both for a reasonable signal-to-noise ratio and discretization error. The effective number allows the number of computational particles to be chosen such that the competing requirements of low computational cost and low statistical uncertainty are balanced. This weight usually remains constant throughout the simulation. Here we note that more sophisticated schemes involving variable weights have been developed for DSMC simulations for cases where the number of particles varies significantly across the simulation domain (e.g., in cylindrical domains[10]). Although partially successful, these methods have not been widely adopted because they exhibit a number of numerical artifacts.[80]

The simulation dynamics are governed by the Boltzmann equation from which stochastic evolution rules for the simulation particles must be derived. These rules follow the basic idea described in Section 2.6, namely that time-integration is split into a collisionless advection substep and a scattering substep.

These substeps are discussed in more detail below after a discussion of the initialization process. Discussion of the scattering substep will be limited to the relaxation-time model on which the vast majority of applications have focused.

3.1 Initialization

Initialization requires the generation of a set of computational particles, N_{part}, that sample the initial condition, namely $f(t = 0, \mathbf{x}, \boldsymbol{\omega}, p)[D(\omega, p)/4\pi]$. We note here that in many cases the problem of interest is steady in time and therefore may not even involve an initial condition as part of its specification. However, as is typical of stochastic particle methods, the method described here is explicit in time and proceeds to integrate forward from an initial condition. In steady problems, the initial condition is typically taken to be some reasonable equilibrium state. We also note that an exception to transient formulations is

the method discussed in Section 6, which provides solutions to steady problems without integrating them explicitly to steady state.

As an example, we consider the case $f(t=0) = f^{\text{eq}}(\omega, T_0)$; then,

$$N_{\text{eff}} = \frac{N}{N_{\text{part}}} = \frac{V}{N_{\text{part}}} \sum_p \int f^{\text{eq}}(\omega, T_0) D(\omega, p) d\omega \tag{33}$$

where N_{part} is the desired number of computational particles in volume V and N is the actual equilibrium number of phonons in that volume.

Samples from a distribution can be generated by calculating and subsequently inverting the cumulative distribution function.[81] In general, this is not possible analytically and is thus typically performed numerically as shown below. We also note that, alternatively, samples from a distribution can be generated using acceptance-rejection. This approach is usually less efficient (due to the rejection step), but more convenient in high dimensions, where numerical integration is cumbersome. An example of acceptance-rejection can be found in Section 4.2. We also note that the ratio-of-uniforms method recently adapted to particle methods for simulating the Boltzmann equation[82] provides improved computational efficiency.

For the example considered here, $f(t=0) = f^{\text{eq}}(\omega, T_0)$ is not easily invertible; thus, the spectral (ω) domain is discretized into bins of width $\Delta\omega$ with central frequencies $\omega_{0,i}$. The number of phonons in each spectral bin is given by

$$\frac{N(\omega_{0,i})}{V} = \sum_p f^{\text{eq}}(\omega_{0,i}, T_0) D(\omega_{0,i}, p) \Delta\omega \tag{34}$$

To choose the bin to which each particle is assigned, a uniformly distributed random number $\mathfrak{R}_1 \in [0,1)$ is drawn and compared to the cumulant distribution function[76,77]

$$F_i = \sum_{j=1}^{i} \frac{N(\omega_{0,j})}{N} \tag{35}$$

The particle is assigned to bin j, such that $F_{j-1} \le \mathfrak{R}_1 < F_j$, and the frequency is distributed randomly in that bin: $\omega = \omega_{0,j} + (2\mathfrak{R}_2 - 1)\Delta\omega/2$, where $\mathfrak{R}_2 \in [0,1)$ is a second uniformly distributed random number. For dispersion relations with multiple branches, the polarization is selected proportional to the number density of phonons from each branch at the chosen frequency (or in the chosen spectral bin). Finally, the phonon traveling direction is sampled; for example, the isotropicity of the equilibrium distribution discussed here results in the following probability functions for the angle distributions:

$$P_1(\theta) = \frac{\sin\theta}{2} \quad \theta \in [0,\pi) \quad \text{and} \quad P_2(\phi) = \frac{1}{2\pi} \quad \phi \in [0, 2\pi) \tag{36}$$

which can be generated from

$$\theta = \cos^{-1}(1 - 2\mathfrak{R}_3) \quad \text{and} \quad \phi = 2\pi\mathfrak{R}_4 \tag{37}$$

where $\mathfrak{R}_3$ and $\mathfrak{R}_4$ are also uniformly distributed random numbers in $[0, 1)$. The sampling step is repeated until the appropriate number of samples has been created (i.e., N_{part}).

3.2 Advection and Boundary Conditions

In the absence of external forces, integration of the advection substep in time amounts to updating the position of each particle using $\mathbf{x}_i(t + \Delta t) = \mathbf{x}_i(t) + \mathbf{V}_{g,i}\Delta t$. Particle advection may lead to interaction with a domain boundary. As a result, boundary condition implementation is also a part of the advection substep. Typical boundary conditions include interactions with physical boundaries (e.g. the interface between two materials) or computational boundaries (e.g., periodic). Some of the most common boundary conditions and their implementations are discussed next.

3.2.1 Isothermal Boundaries

Boundaries at a fixed (known) temperature T_{b} are treated by assuming that phonons leaving the boundary come from the equilibrium distribution $f^{\text{b}} = f^{\text{eq}}(\omega, T_{\text{b}})$. The number flux into the domain is then

$$\dot{N}'' = \sum_p \int V_g(\omega, p) \cos(\theta) f^{\text{eq}}(\omega, T_{\text{b}}) \frac{D(\omega, p)}{4\pi} d^3\boldsymbol{\omega} \tag{38}$$

$$= \frac{1}{4} \sum_p \int V_g(\omega, p) f^{\text{eq}}(\omega, T_{\text{b}}) D(\omega, p) d\omega \tag{39}$$

where $V_g = ||\mathbf{V}_g||$ is the magnitude of the phonon velocity and $0 \leq \theta \leq \pi/2$ is measured from the boundary normal. With $\dot{N}''\mathcal{A}\Delta t/N_{\text{eff}}$ prescribing the number of particles that need to be generated at a boundary of area $\mathcal{A}$ every time step, the procedure from Section 3.1 for drawing the frequencies is repeated except that $f^{\text{eq}}(\omega, T_0)$ is replaced with $V_g(\omega, p) f^{\text{eq}}(\omega, T_{\text{b}})$. Additionally, the probability density functions for the angular distribution of the particle wave vectors can be deduced from the integrand in Eq. (38) as

$$P_1(\theta) = 2\cos\theta\sin\theta \quad \theta \in [0, \pi/2) \quad \text{and} \quad P_2(\phi) = 1/(2\pi) \quad \phi \in [0, 2\pi). \tag{40}$$

Alternatively, an isothermal boundary can be simulated by augmenting the system with a sufficiently large boundary cell in which all particles are reinitialized at the beginning of every timestep.[76] This approach increases the number of particles in the simulation without providing any advantage over the method described above.

3.2.2 Specular and Diffuse Reflections

In specular reflection, a phonon collides with a wall and its postcollision or outgoing wave vector $\mathbf{k}'$ is related to its incoming wave vector $\mathbf{k}$ by

$$\mathbf{k}' = \mathbf{k} - 2\,(\mathbf{k} \cdot \hat{\mathbf{n}})\,\hat{\mathbf{n}} \tag{41}$$

where $\hat{\mathbf{n}}$ is the surface unit normal vector pointing into the material. All other phonon bundle properties are preserved.

A diffuse reflection also conserves phonon energy but randomizes the phonon wave vector isotropically on the unit sphere. This is achieved by drawing the angles θ and ϕ from the angular distributions given in Eq. (40).

The degree of specularity (fraction of specular reflections), d, as a function of the wave vector may be calculated using[23,26,52,83,84]

$$d(\mathbf{k}) = \exp\left(-4k^2\Delta^2\cos\theta_\mathrm{b}\right) \tag{42}$$

where Δ is the root mean square height of the surface roughness and θ_b is the angle between the wave vector and the normal to the boundary. In practice, the specularity may also be (and often is) chosen to match experimental data. For example Volz and Chen found the specular fraction of 0.45 provided good agreement between BTE and molecular dynamics simulations,[85] Mazumder and Majumdar chose a value of 0.6 to match experiments,[77] and Mital and Mazumder proposed 0.885 for 2D thin-film simulations and 0.965 for the 3D thin-film simulations.[86] However, these values of the specularity parameter that provide agreement with externally determined thermal conductivities are also dependent on the dispersion relation and relaxation times.[87] In practice, it is simpler to assume all reflections are isotropically diffuse and recognize that this leads to a lower bound on thermal conductivity. Here we also note that by judicious manipulation of surface characteristics to create backscatter in a preferred direction, MC simulations have shown that the thermal conductivity could be reduced below the limit of completely isotropic diffuse scattering.[22,23] We are not aware of any experimental verification.

3.2.3 Transmission

At the interface between two materials, a phonon may be reflected (as discussed in Section 3.2.2) or transmitted; the transmission can be diffuse or specular, elastic or inelastic. The details of phonon behavior at the interface are not well understood and are still, currently, the object of important research efforts.[88–90] Such interfaces can be modeled using a transmission coefficient, $\mathcal{T}_{12}$, which in a simulation can be interpreted as the probability that a phonon will be transmitted across the interface. If not transmitted, the phonon is reflected (probability $\mathcal{R}_{12} = 1 - \mathcal{T}_{12}$). The probabilities of transmission and reflection can be obtained from physical models, such as the diffuse mismatch model (DMM),[24,25,29] which may be formulated to agree with experimental measurements of thermal boundary conductance.[39,91–93] Because of the clear probabilistic interpretation of $\mathcal{T}_{12}$ and $\mathcal{R}_{12}$, such models are typically readily implemented in MC simulations.

3.3 Scattering

The relaxation-time approximation relies on a model for the scattering rate as a function of frequency, temperature, and polarization. Because of its simple analytic form, Holland's 1963[58] model continues to be popular, and includes isotope scattering

$$\tau_{\text{isotope}}(\omega)^{-1} = A_{\text{isotope}}\omega^4 \tag{43}$$

and normal and umklapp scattering for longitudinal and transverse branches

$$\tau_{\text{LN}}(\omega, T)^{-1} = B_{\text{LN}}\omega^2 T^3 \tag{44}$$

$$\tau_{\text{TN}}(\omega, T)^{-1} = B_{\text{TN}}\omega T^4 \tag{45}$$

$$\tau_{\text{TU}}(\omega, T)^{-1} = \begin{cases} \dfrac{B_{\text{TU}}\omega}{\sinh(\hbar\omega/k_{\text{B}}T)} & \omega_1 < \omega < \omega_2 \\ 0 & \omega < \omega_1 \end{cases} \tag{46}$$

The above functional forms are motivated from limiting behaviors, ω_1 and ω_2 are parameters in Holland's[58] simplified dispersion relation, and the coefficients are optimized to reproduce the bulk temperature–dependent thermal conductivity.

Various scattering models are used in MC schemes ranging from some that completely neglect bulk collisions ($\tau^{-1} = 0$) to study boundaries and low temperatures,[20,22] to those that assume a constant mean free path [$\tau = (\text{const.})$] (the so-called gray model).[24,25,76] Others more faithfully reproduce Holland's model,[35,77,79,94,95] while some reoptimize the coefficients and exponents.[28,87,96] Frequency-dependent simulations in this chapter will be based on the latter with parameters from Ref. 97.

Putting aside for a moment the fact that the relaxation time is an approximation, comparison to experiments and ab initio simulations as a means of determining relaxation times shows that the latter are strongly frequency-dependent. This casts serious doubt on the value of the gray model in particular, which by assuming a frequency-independent relaxation time, significantly underestimates the strength of ballistic effects. For example, in silicon, the product $V_g(\omega p)\tau(\omega p)$ spans length scales from nanometers to tens of microns.[28] More generally, a Knudsen number based on the mean free path will obscure the fact that individual phonon modes may travel significantly longer than $L\,\text{Kn}$ without interactions (ballistically).

Optical phonons, which are notably absent from Holland's model, tend to have a small group velocity and correspondingly small contribution to thermal conductivity. Nevertheless, these phonons can have a significant capacitive effect in transient problems.[39] A scheme that includes the contribution of optical phonons and more details about allowed branch conversions was also developed[78] and used in the MC context.[86] For details on the latter, the reader is referred to these references. Another simpler scheme for including optical branches is given in Refs. 39 and 97.

The probability of a particle undergoing a scattering event during the time step Δt is calculated from

$$P(\omega, p, T) = 1 - \exp\left[\frac{-\Delta t}{\tau_{\text{total}}(\omega, p, T)}\right] \tag{47}$$

where $\tau_{\text{total}}^{-1} = \sum_i \tau_i^{-1}$, with the sum running over all scattering modes described by Eqs. (43)–(46) or the selected model. When a particle is selected for collision, a uniformly distributed random number $\mathfrak{R}$ is drawn in $[0, 1)$ and the specific collision type j is chosen such that $\sum_{i=1}^{j-1} \tau_i^{-1}\tau_{\text{total}} \le \mathfrak{R} < \sum_{i=1}^{j} \tau_i^{-1}\tau_{\text{total}}$. If a two-phonon processes (e.g., impurity

scattering) is selected, the traveling direction of a phonon is randomized, but its frequency and wave vector magnitude are unchanged.

Three phonon scattering is more complex. Particles are deleted based on their relaxation time and new particles are drawn from the appropriate local equilibrium distribution $f^{\text{loc}} = f^{\text{eq}}(\omega, \tilde{T})$, which to conserve energy must satisfy[79]

$$\sum_p \int \frac{\hbar\omega f(t,\mathbf{x},\boldsymbol{\omega},p)}{\tau(\omega,p,T)} \frac{D(\omega,p)}{4\pi} d^3\boldsymbol{\omega} = \sum_p \int \frac{\hbar\omega f^{\text{eq}}(\omega,\tilde{T})}{\tau(\omega,p,T)} D(\omega,p) d\omega \tag{48}$$

Equation (48) defines the scattering pseudo-temperature $\tilde{T}(t,\mathbf{x})$, while $T(t,\mathbf{x})$ is determined from (16). When the relaxation time is not a function of frequency and polarization, the pseudo-temperature is equal to the local temperature $\tilde{T} = T$, and phonons can be drawn from the local equilibrium distribution as in the initialization procedure of Section 3.1. Otherwise, particles must be drawn from

$$\frac{f^{\text{eq}}(\omega,\tilde{T})}{\tau(\omega,p,T)} D(\omega,p) \tag{49}$$

Note that, as discussed in Section 3.4, in MC simulations the values of T and $\tilde{T}$ are typically recovered by averaging particle contributions over finite regions of space (cells). Therefore, in practice, Eqs. (16) and (48) are imposed in a cell-average sense.

The traveling direction of a scattered particle is randomized, which "approximates" the overall lack of momentum conservation in three phonon processes. Attempts have been made to preserve the momentum-conserving nature of the normal processes, (e.g., Ref. 79), but because the underlying scattering times were developed in a scheme that cannot properly distinguish between the normal and umklapp processes,[58] correctly treating the momentum conservation of normal processes in MC could actually drive the solution for thermal conductivity away from the accepted values.[28]

Ultimately, the basic scattering algorithm described above does not strictly conserve energy. Even though scattered phonon frequencies are drawn from Eq. (49), which has the correct expectation value of temperature (energy), the energy of the (small number) of scattered phonons within each cell is just a sample of this distribution with an energy that fluctuates about the expectation. This means that the energy of the simulation is not a constant of the motion, but rather it fluctuates about the expected value. These fluctuations, believed to be random walks, are undesirable because they increase statistical uncertainty, but also because they have the potential to (non linearly) interact with other fluctuating processes in the simulation, resulting in bias.

Random walks are inherently a finite sampling effect, and their magnitude can be decreased by increasing the number of computational particles (minimizing the stochastic noise). However, because the latter increases computational cost (and storage), various algorithms have been proposed for keeping random walks under control using alternative means. One example includes the creation of additional particles or the deletion of already created particles until the postscattering energy is within an acceptable tolerance of the prescattering energy.[42,77] This approach reduces the magnitude of the random walks, but

it does not eliminate them. Moreover, it biases the distribution of phonons in ways that have yet to be analyzed. Another approach amounts to tracking the deficit in the energy after each scattering event and carrying the deficit forward to subsequent time steps.[82] This approach has also been used in connection to the generation of phonons at a material interface.[24] The latter approach reduces random walks considerably but is still far from ideal because its effect on the simulation accuracy is not known.

3.4 Energy-Based Formulations

It was recently shown[61] that exact energy conservation can be achieved by simulating the energy-based Boltzmann equation

$$\frac{\partial e}{\partial t} + \mathbf{V}_g \cdot \nabla_{\mathbf{x}} e = \frac{e^{\text{loc}} - e}{\tau(\omega, p, T)} \tag{50}$$

obtained by multiplying the BTE by $\hbar\omega$ and defining $e = \hbar\omega f$ and $e^{\text{loc}} = \hbar\omega f^{\text{loc}}$. The basic idea behind this formulation is that each computational particle "carries" a fixed amount of energy, $\mathcal{E}_{\text{eff}}$, rather than an effective number of phonons. In other words, these computational particles can no longer be thought of as phonon bundles. As a result of this formulation, energy conservation becomes equivalent with particle conservation, which can be enforced exactly, ensuring no truncation or other forms of discretization error in this regard.

The procedures for simulating this equation follow directly by modifying the discussion of this chapter to particles representing the quantity $e = \hbar\omega f$ instead of f. More details can be found in Section 4.2 where the energy-based formulation is combined with a control-variate variance-reduction formulation as originally proposed in Ref. 61.

3.5 Statistical Sampling

To capture the spatial dependence of the solution field, the simulation domain is typically discretized into cells (ideally, many in each dimension) and local properties are calculated as cell-based averages. For example, the cell-based average of property A is defined as $A_{\text{cell}} = (1/V)\int_{\mathbf{x}\in V} A d^3\mathbf{x}$, where V denotes the volume of the cell. Substituting the particle representation of the distribution function and performing the volume integration, leads to the estimator $\bar{A} = (N_{\text{eff}}/V)\sum_i A_i$, where A_i denotes the contribution of particle i to the quantity A; in the interest of simplicity, here and in what follows, the subscript "cell" will be omitted from the estimator symbol.

Following this procedure for the number density, energy density, and heat flux—namely, substituting the particle representation (32) in (12)–(14) and performing the volume average—we obtain

$$\bar{n} = \frac{N_{\text{eff}}}{V}\sum_i 1, \quad \bar{U} = \frac{N_{\text{eff}}}{V}\sum_i \hbar\omega_i, \quad \bar{\mathbf{q}}'' = \frac{N_{\text{eff}}}{V}\sum_i \hbar\omega_i \mathbf{V}_{g,i} \tag{51}$$

Knowledge of the statistical uncertainty as a function of the number of simulation particles is very useful for providing confidence intervals for simulation results, but also for a priori estimating the computational resources required for a simulation and appropriately choosing N_{eff}. Although estimates of the statistical uncertainty of typical moments of interest have been provided for the case of DSMC,[7] the unique features of phonon simulations (wave vector, frequency, density of states) make these more difficult to obtain analytically. Here we calculate the statistical uncertainty for the gray Debye model for which semianalytical results are possible. As we show in Section 4.3, the estimates provided here are sufficiently accurate to serve as reasonable guidelines for more complex material models.

Let us consider a Debye material with N_{atoms} atoms per volume V, in which $\omega = v_{\text{D}}k$, $\hbar v_{\text{D}} k_{\text{D}} = k_{\text{B}}\Theta_{\text{D}}$, $k_{\text{D}} = (6\pi^2 N_{\text{atoms}}/V)^{(1/3)}$, and $\tau = (\text{const.})$.

Following previous work,[7] we will calculate the variance of estimators using equilibrium distributions. The latter approximation is necessary because the nonequilibrium distribution is not known, but also justified since for the application of interest here the contribution of the deviation from equilibrium to fluctuations is small. The rationale for this is further discussed in Section 2.5.

At equilibrium and according to the Debye model, the number density of phonons is given by

$$n_0 = \frac{3}{2\pi^2}\left(\frac{k_{\text{B}}T}{\hbar v_{\text{D}}}\right)^3 I_2\left(\frac{\Theta_{\text{D}}}{T}\right) \tag{52}$$

where $I_n(x_{\text{max}}) = \int_0^{x_{\text{max}}} [x^n/(e^x - 1)]dx$, while the energy density is given by

$$U_0 = \frac{3}{2\pi^2}\frac{(k_{\text{B}}T)^4}{(\hbar v_{\text{D}})^3} I_3\left(\frac{\Theta_{\text{D}}}{T}\right) \tag{53}$$

There are at least two approaches for calculating the statistical uncertainty associated with estimators such as the ones in Eq. (51): the first is to calculate the equilibrium fluctuations of the properties of interest [e.g., Eqs. (52) and (53)] and then to use the central limit theorem to calculate the uncertainty of the estimator based on the number of samples.[7] The second, which is the one taken here, is to directly calculate the variance of the estimator.

Let Y be a random variable that represents the number of computational particles in the volume V. Because of the phonon gas assumption, Y is Poisson distributed,[7] and recalling that $N_{\text{part}} = n_0 V/N_{\text{eff}}$, the expected value and variance of Y are equal to

$$\text{E}[Y] = \text{var}(Y) = N_{\text{part}} \tag{54}$$

Implementation of boundary conditions may affect the underlying distribution of particles; thus, we note that the following is only strictly true sufficiently far away from the boundaries.

The frequency of a phonon can also be modeled by a random variable, hence the total energy is the sum of a random number of random variables, and its variance can be calculated by

$$\text{var}(\bar{U}) = \text{var}\left(\frac{N_{\text{eff}}}{V}\sum_{i=1}^{Y}\hbar\omega_i\right) = \frac{N_{\text{eff}}^2}{V^2}\left[\text{E}[Y]\text{var}(\hbar\omega) + \text{E}[\hbar\omega]^2\text{var}(Y)\right] \tag{55}$$

$$= \frac{N_{\text{eff}}^2}{V^2}N_{\text{part}}\text{E}[(\hbar\omega)^2] \tag{56}$$

The expected value in this expression is given in the equilibrium approximation by

$$\begin{aligned}\text{E}[(\hbar\omega)^2] &= \frac{1}{n_0}\sum_p\int(\hbar\omega)^2 f^{\text{eq}}(\omega,T)D(\omega,p)d\omega \\ &= (k_{\text{B}}T)^2\,\frac{I_4\left(\Theta_{\text{D}}/T\right)}{I_2\left(\Theta_{\text{D}}/T\right)}\end{aligned} \tag{57}$$

The statistical uncertainty associated with the measurement of the energy in a cell of volume V that contains on average N_{part} particles is thus given by

$$\sigma_{\bar{U}} = \frac{n_0 k_{\text{B}}T}{\sqrt{N_{\text{part}}}}\sqrt{\frac{I_4\left(\Theta_{\text{D}}/T\right)}{I_2\left(\Theta_{\text{D}}/T\right)}} \tag{58}$$

These results allow us to estimate the uncertainty in temperature measurements $\bar{T}$ using $\sigma_{\bar{T}} \approx [1/C(T)\sigma_{\bar{U}}]$, where

$$C(T) = \frac{\partial U}{\partial T} = \frac{3k_{\text{B}}}{2\pi^2}\left(\frac{k_{\text{B}}T}{\hbar v_{\text{D}}}\right)^3\int_0^{\Theta_D/T}\frac{x^4e^x}{\left(e^x-1\right)^2}dx \tag{59}$$

If we define $J_4(x_{\text{max}}) = \int_0^{x_{\text{max}}}[x^4e^x/(e^x-1)^2]dx$, then

$$\sigma_{\bar{T}} = \frac{T}{\sqrt{N_{\text{part}}}}\frac{\sqrt{I_4\left(\Theta_{\text{D}}/T\right)I_2\left(\Theta_{\text{D}}/T\right)}}{J_4\left(\Theta_{\text{D}}/T\right)} \tag{60}$$

Finally, the variance in the equilibrium heat flux in a single direction is given by

$$\text{var}\left[\frac{N_{\text{eff}}}{V}\sum_{i=1}^{Y}\hbar\omega_i v_{\text{D}}\cos(\theta_i)\right] = \frac{N_{\text{eff}}^2N_{\text{part}}}{V^2}\text{E}[(\hbar\omega v_{\text{D}}\cos\theta)^2] \tag{61}$$

with

$$\begin{aligned}\text{E}[(\hbar\omega v_{\text{D}}\cos\theta)^2] &= \frac{1}{n_0}\sum_p\int\int\int\left(\hbar\omega v_{\text{D}}\cos(\theta)\right)^2 f^{\text{eq}}(\omega,T)\frac{D(\omega,p)}{4\pi}\sin\theta d\omega d\theta d\phi \\ &= \frac{v_{\text{D}}^2}{3}\left(k_{\text{B}}T\right)^2\frac{I_4\left(\Theta_{\text{D}}/T\right)}{I_2\left(\Theta_{\text{D}}/T\right)}\end{aligned} \tag{62}$$

This yields the following expression for the statistical uncertainty in the heat flux estimator:

$$\sigma_{\bar{q}_x''} = \frac{n_0 v_\mathrm{D} k_\mathrm{B} T}{\sqrt{N_\mathrm{part}}} \sqrt{\frac{I_4\left(\Theta_\mathrm{D}/T\right)}{3 I_2\left(\Theta_\mathrm{D}/T\right)}} \tag{63}$$

These uncertainties all have in common the $1/\sqrt{N_\mathrm{part}}$ dependence—the characteristic signature of statistical sampling. This dependence makes it particularly challenging to resolve low signal problems such as those typically found in micro- and nanoscale devices. This is further discussed in Section 4.

We also note here that the energy-based formulation of Section 3.4 leads to simpler estimates for and slightly smaller values of fluctuations in energy and heat flux. In this case, the local properties are measured by

$$\bar{U} = \frac{\mathcal{E}_\mathrm{eff}}{V} \sum_i 1 \quad \text{and} \quad \bar{\mathbf{q}}'' = \frac{\mathcal{E}_\mathrm{eff}}{V} \sum_i \mathbf{V}_{g,i} \tag{64}$$

Under the assumptions of the preceding analysis (Debye, gray) the variance of these quantities is then given by

$$\mathrm{var}(\bar{U}) = \mathrm{var}\left(\frac{\mathcal{E}_\mathrm{eff}}{V} \sum_{i=1}^{Y} 1\right) = \frac{\mathcal{E}_\mathrm{eff}^2}{V^2} N_\mathrm{part} \tag{65}$$

and by

$$\mathrm{var}\left(\bar{q_x}''\right) = \mathrm{var}\left(\frac{\mathcal{E}_\mathrm{eff}}{V} \sum_{i=1}^{Y} v_\mathrm{D} \cos(\theta_i)\right) = \frac{\mathcal{E}_\mathrm{eff}^2 v_\mathrm{D}^2 N_\mathrm{part}}{V^2} \mathrm{E}[\cos^2\theta] = \frac{\mathcal{E}_\mathrm{eff}^2 v_\mathrm{D}^2 N_\mathrm{part}}{3V^2} \tag{66}$$

Accordingly, the uncertainty in the heat flux for the energy-based formulation can be calculated as follows:

$$\sigma_{\bar{q}_x''} = \frac{U_0 v_\mathrm{D}}{\sqrt{3 N_\mathrm{part}}} \tag{67}$$

This quantity varies between 83% and 95% of Eq. (63) (as a function of temperature), because in the energy-based formulation, there is no fluctuation in the amount of energy a particle carries.

The results derived above are in very good agreement with MC simulations (not shown here) of the same model (Debye, gray). Figure 2 shows a comparison to simulations of the more realistic material model used in Ref. 61. The figure compares the theoretical results for the relative statistical uncertainty in the heat flux to those obtained from simulating heat transfer between two plates at different temperatures as a function of the temperature difference between the two plates. In this figure, the statistical uncertainty of each material model is normalized by the heat flux predicted by the model; more details on the simulations can be found in Section 4.3. The figure shows that, provided the statistical uncertainty is normalized by the heat flux predicted by the model in question, the agreement between the fluctuation results derived above and simulations is very satisfactory. This suggests that

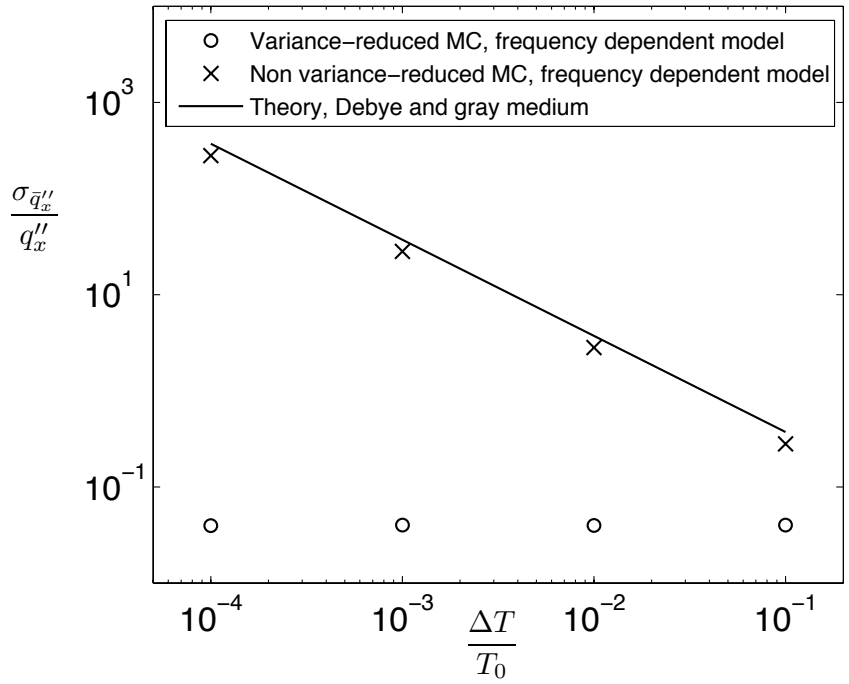

FIG. 2: Ratio $\sigma_{\bar{q}_x''}/q_x''$ as a function of $\Delta T/T_0$.

the theoretical results developed here provide reasonable guidelines for general material models (provided deviations from equilibrium are small).

3.6 Deterministic Numerical Error

In addition to statistical uncertainty, MC methods of the type discussed here are expected to suffer from discretization error due to discretization in the time, space, and frequency [e.g., see Eq. (34)] domains.

In the time-split algorithms discussed here, second-order accuracy in time is only obtained if the splitting is symmetric in time.[68,71,74] This requires that the sampling process be inserted in the middle of a scattering or an advection event.[82] In DSMC algorithms, it has been shown that it is also possible to achieve second-order behavior by sampling twice during a time step (before and after scattering or advection).[74] Finally, we note that here we are referring to the error due to splitting the integration into a scattering and an advection event. Additional error will be incurred by the integration of Eq. (31) within each cell, unless an algorithm with no error is used.[64,98]

The error due to finite cell size has not been analyzed for phonon Monte Carlo methods, although this may be expected to be qualitatively similar to the error in DSMC algorithms discussed in Section 2.6. The error due to a finite number of particles has also not been characterized; it is currently not clear whether this error is qualitatively similar to that in DSMC because the number of particles in the standard phonon MC method described here is not conserved. The error due to spectral discretization has been shown to converge

to acceptable levels for ∼1000 spectral bins,[86] but rigorous analysis of this effect is also lacking.

3.7 Imposing a Constant Temperature Gradient in Periodic Simulations

Periodically nanostructured materials are seen as a potentially effective way of designing high-performance thermoelectric materials.[99] Simulation of periodic structures under an external temperature gradient is essential for the calculation of the effective thermal conductivity of nanocomposites. In such calculations, significant efficiency gains can be achieved by simulating only one period (unit cell) of the structure and imposing periodic boundary conditions (e.g., see Fig. 3). However, periodic boundary conditions in their typical implementation do not allow for the presence of a temperature gradient.

An approach to overcome this was developed by Jeng et al.[24] and later refined by Hao et al.[28] The fundamental assumption in their approach is that periodicity in the presence of a temperature gradient can be reproduced by requiring the deviation from local equilibrium to be periodic; in the nomenclature of Fig. 3, this can be written as

$$f(t, x_1, y, z, \boldsymbol{\omega}, p) - f^{\text{eq}}(\omega, T_1) = f(t, x_2, y, z, \boldsymbol{\omega}, p) - f^{\text{eq}}(\omega, T_2) \tag{68}$$

This requirement is consistent with homogenization-type approaches,[100] in which periodicity over the unit cell is assumed to be a result of the small size of the unit cell compared to the characteristic scale of variation of the externally imposed temperature gradient. More specifically, the above relation can be obtained[101] from a first-order expansion in the parameter defined as the ratio of the unit cell size in the direction of the temperature gradient to the characteristic scale of variation of the externally imposed temperature gradient.

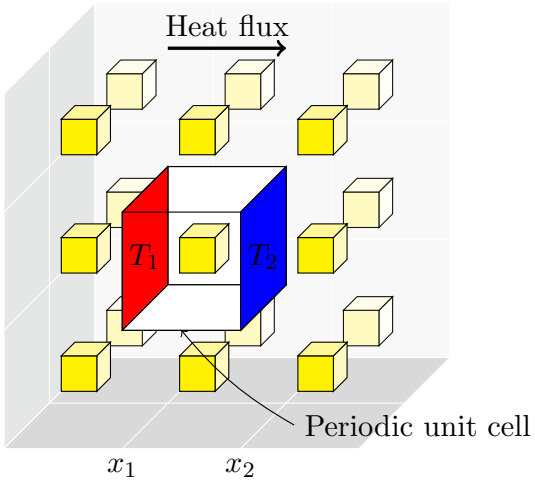

FIG. 3: Nanocomposite formed of a pattern of rectangular second phase inclusions distributed in a semiconducting matrix (not shown). A single unit cell with an applied temperature difference ($T_2 - T_1$) can be used to significantly decrease the computational domain when simulating periodic nanocomposites.

Implementation of condition (68) requires deletion of particles exiting the domain at $x = x_2$ and introduction of particles at $x = x_1$ moving in the positive direction that sample the distribution

$$f^+(t, x_1, y, z, \boldsymbol{\omega}, p) = f^+(t, x_2, y, z, \boldsymbol{\omega}, p) - f^{\text{eq}}(\omega, T_2) + f^{\text{eq}}(\omega, T_1) \qquad (69)$$

The most straightforward method to sample from this distribution begins[28] by collecting the pool of particles leaving the domain at $x = x_2$. In traditional periodic boundary conditions, this entire pool would be reintroduced at $x = x_1$ satisfying $f^+(t, x_1, y, z, \boldsymbol{\omega}, p) = f^+(t, x_2, y, z, \boldsymbol{\omega}, p)$. To satisfy Eqs. (69), one must modify this pool by deleting particles according to the distribution $f^{\text{eq}}(\omega, T_2)$ and introducing new particles that sample $f^{\text{eq}}(\omega, T_1)$. In order to remove particles from $f^{\text{eq}}(\omega, T_2)$, a new set of particles must be sampled from this distribution and then the particles in the pool that are most similar to the newly sampled particles can be deleted. Particles leaving the domain at $x = x_1$ can be treated analogously.

This approach introduces an unknown amount of error because the particles crossing periodic boundaries will not correspond exactly to the particles that are sampled to guide the deletion process. Fortunately, an alternative formulation discussed in Section 4.2 based on deviations from equilibrium is naturally suited to simulating Eq. (68) exactly, because it allows for negative particles.

3.8 Beyond the Relaxation-Time Model

The difficulty associated with solution of the more complete BTE with the ab initio scattering operator (10) lies in the computational cost required for recovering the possible pathways associated with a particular scattering process ($\mathbf{k} \rightarrow \mathbf{k}' + \mathbf{k}''$ or $\mathbf{k} + \mathbf{k}' \rightarrow \mathbf{k}''$) and the calculation of the matrix elements associated with the Hamiltonian of interaction (e.g., $\mathcal{Q}_{\mathbf{k}p}^{\mathbf{k}'p',\mathbf{k}''p''}$ of (10)). Additionally, because the functional form of this scattering operator differs significantly from the traditional operators (e.g., hard-sphere and its variants[10]), until recently, MC procedures for efficiently sampling scattering events appropriately (at the correct relative rates) were not available. As a result, solutions of the Boltzmann equation involving this operator addressed primarily the space-homogeneous, time-independent problem associated with determining the thermal conductivity of (homogeneous) semiconductors, using deterministic iterative schemes.[51,102–104]

Some recent work attempting to improve the performance of MC solution methods has focused on determining the scattering rates from molecular dynamics and density functional theory–for example Refs. 96 and 105–108. Although these can be used to inform the relaxation-time model,[28] which appears to capture the decay of out of equilibrium modes reasonably well,[109–111] ultimately, single mode relaxation-time models fail to capture important couplings between modes.[112–114] This, has long been cited as a limitation of the MC approach,[115,116] because MC methods, unjustifiably, have been historically identified with the relaxation-time approximation.

For the reasons discussed in Section 2.6, an MC approach for solving problems of engineering interest using scattering operator (10) to describe phonon interactions is expected

to be simpler and more efficient than an extension of the existing deterministic solution methods[51,102–104] to temporally and spatially varying problems. To this end, Garcia and Wagner have developed an extension of DSMC for the Uehling-Uhlenbeck scattering operator that obeys Bose-Einstein (as well as Fermi-Dirac) statistics.[117] While this method correctly treats momentum and energy conservation, the scattering model clearly does not model three-phonon interactions; moreover, the resulting algorithm requires reconstruction of the distribution from its samples, which is very inefficient and negates one of the main advantages of DSMC, namely the ability to simulate these processes without reconstructing the distribution function from its samples. Other models that attempt to account for momentum and energy conservation, but fail to completely consider the Hamiltonian of interaction (or scattering kernel) and introduce approximations that are difficult to justify, have also been proposed.[94,118,119] We also mention Hamzeh and Aniel, who employed a scheme similar to that of Ref. 51 to calculate the transition probability for each pathway and a generalized Ridley scheme to estimate the transition probability (in terms of the Grüneisen parameter). This study was limited to spatially homogeneous systems.

Recently, a deviational formulation for solving the BTE with ab initio scattering for spatially and temporally varying problems in two dimensions has been proposed, validated and used to study phonon transport in graphene ribbons.[46,47] The proposed formulation uses a discretized representation of reciprocal space as a means of evaluating (10) and uses force constants (scattering rates) derived from density functional theory. With the exception of the scattering substep which is very different, the discrete reciprocal space requires only small changes to the other aspects of the deviational formulation as described in Section 4. More details can be found in Refs. 46 and 47.

4. DEVIATIONAL METHODS AND VARIANCE REDUCTION

As shown in Section 3.5 and more generally in Ref. 7, the statistical uncertainty in the estimator $\bar{A}$ of a quantity of interest A (e.g., heat flux) is of the form $\sigma_{\bar{A}} = \sqrt{C_A/N}$, where N is the number of independent samples used to calculate the estimate $\bar{A}$; C_A can be thought of as the variance associated with the particle population used to calculate A. For traditional Monte Carlo methods where particles simulate the complete distribution function, C_A can be identified as the population variance associated with the phonon distribution. A direct consequence of this result is that as $A \to 0$, C_A is the population variance associated with equilibrium and is independent of the magnitude of A. As a result, $\sigma_{\bar{A}}/A \to \infty$ for fixed N, or alternatively, for a fixed signal-to-noise ratio, as A decreases, N needs to increase as A^{-2}.

This limitation is particularly important in the context of micro-/nanoscale science and technology applications where kinetic effects are important due to small length scales rather than large temperature differences. Examples include the transient thermoreflectance technique,[120–123] which has recently received renewed attention as a potential tool for measuring phonon mean free paths.[40,41] In this technique, a laser pulse induces a local temperature difference on the order of 1K, which then decays through transport by several orders of magnitude. Resolution of these small temperature differences is impossible by regular MC simulations; using Eq. (60), the Debye model predicts that to resolve a temperature

difference of 1 K with a signal to noise ratio of 100, we need nearly $N = 3 \times 10^8$ independent samples per computational cell, which is clearly intractable. Another example of problems of recent practical interest is the calculation of the "effective thermal conductivity" of nanostructured materials.[24] In these simulations, small temperature differences must be used, since large temperature differences will result in a non-linear response.

In the sections that follow, we discuss a class of formulations that address this limitation by drastically reducing the statistical uncertainty of Monte Carlo methods. By adapting the concept of control variates to the stochastic integration of the Boltzmann equation for the purpose of removing the variance associated with the equilibrium part of the distribution, these formulations result in a method which in the small A limit is characterized by $\sqrt{C_A} = \alpha A$, with α constant and much smaller than $\sqrt{\text{var}(A)}/A$. This has two consequences: first, the relative uncertainty $\sigma_{\bar{A}}/A$ is now independent of A, leading to simulation methods that can capture arbitrarily low signals at a cost that does not increase with a decreasing A; second, this constant cost is small making such problems not only tractable but also efficient to treat.[124]

These methods, referred to as deviational, were first introduced in the context of dilute gases and the DSMC method.[67,125] Since then, they have been adapted to phonon transport[61] and extended to improve their performance. In the rest of this section, we discuss these methods and their extensions in detail.

4.1 Control Variates

The variance reduction approach described here is based on the general idea of control variates which can be explained using the following identity

$$\int A(\Gamma) f(\Gamma) d\Gamma = \int A(\Gamma)[f(\Gamma) - g(\Gamma)] d\Gamma + \int A(\Gamma) g(\Gamma) d\Gamma \tag{70}$$

Here, the function $g(\Gamma)$ (the control) is chosen such that

- $g(\Gamma)$ captures most of the variation of $f(\Gamma)$ [i.e., $g(\Gamma) \approx f(\Gamma)$]
- $\int A(\Gamma) g(\Gamma) d\Gamma$ can be deterministically (analytically or otherwise) evaluated

Using a Monte Carlo method to evaluate only $\int A(\Gamma)[f(\Gamma) - g(\Gamma)] d\Gamma$ results in significantly reduced statistical uncertainty, because an appropriately selected $g(\Gamma)$ makes the latter term and its corresponding statistical uncertainty small. The deterministic evaluation of $\int A(\Gamma) g(\Gamma) d\Gamma$ provides the remainder of the integration without stochastic noise.[1]

4.2 Deviational Monte Carlo Method

The control-variate formulation lends itself naturally to the MC methods considered here, because the control $g(\Gamma)$ can be readily identified as a nearby equilibrium distribution $f^{\text{eq}}(\omega, T_{\text{eq}})$ [i.e., Eq. (15)], whose moments are known semi-analytically. This results in a simulation method that solves for the deviation from equilibrium $f^{\text{d}} = f - f^{\text{eq}}_{T_{\text{eq}}}$, while the

contribution of equilibrium to the properties of interest is added deterministically. To simplify the notation, in what follows we will use f_T^{eq} to denote the Bose-Einstein distribution evaluated at a temperature T. In previous sections, this function was denoted by $f^{\text{eq}}(\omega, T)$.

These "deviational" methods differ minimally from the standard methods discussed in Section 3, yet deliver significant computational benefits in the small-signal limit because they address the root of the problem. Low-signal-to-noise ratios in MC simulations are typically the symptom of small deviation from equilibrium [in the sense of small characteristic temperature difference ΔT and not a small deviation from the local equilibrium (see Section 2.5 for a discussion)]. We also emphasize that Eq. (70) on which these methods are based is exact. In other words, no approximation is committed by simulating the deviation from equilibrium (provided the contribution of equilibrium is also accounted for). On the other hand, the resulting computational efficiency will depend on the choice of the equilibrium distribution (control). The closer $f_{T_{\text{eq}}}^{\text{eq}}$ is to f, the greater the computational benefit. Methods that exploit this observation are discussed in Section 5.

As discussed in Ref. 61 and Section 3.4, simulating $e^{\text{d}} = \hbar\omega f^{\text{d}} = e - e_{T_{\text{eq}}}^{\text{eq}}$, lends itself naturally to implementation of exact energy conservation, making this the preferred formulation. The function e^{d} obeys the energy-based deviational Boltzmann equation

$$\frac{\partial e^{\text{d}}}{\partial t} + \mathbf{V}_g \cdot \nabla_{\mathbf{x}} e^{\text{d}} = \frac{e^{\text{loc}} - e_{T_{\text{eq}}}^{\text{eq}} - e^{\text{d}}}{\tau(\omega, p, T)} \tag{71}$$

The similarity of Eq. (71) to the original Boltzmann equation (in the relaxation-time approximation) ensures that the deviational algorithm is not significantly different from the one discussed in Section 3. Time integration proceeds using a splitting algorithm with time step Δt. The choice of T_{eq} is fairly arbitrary, provided the resulting deviations from $e_{T_{\text{eq}}}^{\text{eq}}$ are small (if deviations from equilibrium are small, any convenient temperature value T'_{eq} within the computational domain will be sufficiently close to T_{eq} that deviations from $e_{T'_{\text{eq}}}^{\text{eq}}$ will also be small).

Simulation by particles corresponds to the approximation $e^{\text{d}} D/(4\pi) = \mathcal{E}_{\text{eff}}^{\text{d}} \sum_i s_i \delta^3(\mathbf{x} - \mathbf{x}_i)\delta^3(\boldsymbol{\omega} - \boldsymbol{\omega_i})\delta_{p,p_i}$, where s_i is a sign parameter, made necessary because e^{d} can be a negative quantity and where computational particles represent fixed amounts of deviational energy denoted $\mathcal{E}_{\text{eff}}^{\text{d}}$. The latter quantity is also defined at the start of the simulation; it is determined by balancing the competing requirements of low statistical uncertainty and low computational cost, although the approach is problem dependent. For example, if one wishes to initialize a simulation with N_{init} particles, then given the initial condition $f^{\text{i}}(t = 0, \mathbf{x}, \boldsymbol{\omega}, p)$, $\mathcal{E}_{\text{eff}}^{\text{d}}$ is determined from

$$\mathcal{E}_{\text{eff}}^{\text{d}} = \frac{1}{N_{\text{init}}} \int \int \sum_p \frac{D\hbar\omega(f^{\text{i}} - f_{T_{\text{eq}}}^{\text{eq}})}{4\pi} d^3\boldsymbol{\omega} d^3\mathbf{x} \tag{72}$$

provided that f^{i} differs from the chosen equilibrium. If $f^{\text{i}} = f_{T_{\text{eq}}}^{\text{eq}}$ (usually by choice in steady-state problems, to simplify initialization) an alternative—and more general—way of proceeding consists of calculating the total deviational energy involved in the simulation

(namely, the total deviational energy associated with the initial condition, added to the energies derived from the boundary and volume sources integrated in time). Dividing this quantity by the desired total number of particles yields the value of the effective deviational energy.

Here, we summarize the main differences between the traditional Monte Carlo algorithm discussed in Section 3 and the deviational algorithm (more details can be found in Ref. 61):

1. Because e^{d} can be positive or negative, a new degree of freedom, the particle sign, is introduced.

2. The particles introduced in the system at the initialization step are drawn from the deviational initial distribution $e^{\mathrm{i}} - e^{\mathrm{eq}}_{T_{\mathrm{eq}}}$.

3. The cell-based temperature is obtained by calculating the deviational energy density $U^{\mathrm{d}}_{\mathrm{cell}} = \mathcal{E}^{\mathrm{d}}_{\mathrm{eff}}(N^+ - N^-)/V_{\mathrm{cell}}$, where N^+ and N^- respectively refer to the number of positive and negative computational particles in the cell of volume V_{cell}. The temperature is then obtained by finding T such that

$$U^{\mathrm{d}}_{\mathrm{cell}} = \int_{\omega} \sum_{p} D(\omega, p)\hbar\omega \left[\frac{1}{\exp\left(\hbar\omega/k_{\mathrm{B}}T\right) - 1} - \frac{1}{\exp\left(\hbar\omega/k_{\mathrm{B}}T_{\mathrm{eq}}\right) - 1} \right] d\omega \quad (73)$$

The pseudo-temperature, defined by the energy conservation statement (48) written here in deviational form

$$\int_{\omega} \sum_{p} \frac{D(\omega, p)(e^{\mathrm{eq}}_{\tilde{T}} - e^{\mathrm{eq}}_{T_{\mathrm{eq}}})}{\tau(\omega, p, T)} d\omega = \int_{\boldsymbol{\omega}} \sum_{p} \frac{D(\omega, p)e^{\mathrm{d}}}{4\pi\tau(\omega, p, T)} d^3\boldsymbol{\omega} \quad (74)$$

is similarly evaluated.

4. Particles to be scattered are chosen based on their respective frequency-dependent scattering rates. Postcollision properties are then drawn from the deviational distribution

$$\frac{\hbar\omega D(\omega, p)}{4\pi\tau(\omega, p, T)} \left[\frac{1}{\exp\left(\hbar\omega/k_{\mathrm{B}}\tilde{T}\right) - 1} - \frac{1}{\exp\left(\hbar\omega/k_{\mathrm{B}}T_{\mathrm{eq}}\right) - 1} \right] \quad (75)$$

Drawing particles from such a distribution can be tedious; computing for each time step and for each cell the approximate cumulative distribution is computationally costly. One can, instead, compute and store at the start of the simulation the cumulative distribution function corresponding to Eq. (75) for $T = \tilde{T} = T_{\mathrm{max}}$, where T_{max} is greater than the highest expected temperature in the system. Then, by drawing frequencies and polarizations from this distribution and using an acceptance-rejection scheme, one can draw samples corresponding to Eq. (75) without having to recompute the cumulative distribution at the current local temperatures.

5. A deletion scheme can be implemented in order to prevent uncontrolled growth of the number of particles in the simulation. The deletion process takes advantage of the fact that energy conservation only requires the net amount of energy to be conserved during scattering. In other words, positive and negative particles selected for deletion may be cancelled and only the net number of particles (of the appropriate sign) need be generated. Some boundary conditions (e.g., isothermal boundaries) also contribute to particle cancellation by allowing cancellation of particles incident upon them. More details can be found in Ref. 61.

6. Boundary conditions can usually be written in terms of deviational distributions making their interpretation analogous to the standard cases discussed in Section 3. For instance, emission of deviational particles from an isothermal boundary at temperature T_b follows the development of Section 3.2.1 with the Bose-Einstein distribution $f^\mathrm{eq}_{T_\mathrm{b}}$ replaced by $\hbar\omega(f^\mathrm{eq}_{T_\mathrm{b}} - f^\mathrm{eq}_{T_\mathrm{eq}})$. Because the Bose-Einstein distribution is monotonic, the sign of the emitted particles is the same as the sign of the difference $T_\mathrm{b} - T_\mathrm{eq}$.

4.3 Computational Gain

In this section we use an archetypal 1D problem, namely steady-state, cross-plane heat transfer in a nanofilm bounded by two isothermal walls at temperatures T_l and T_r, respectively,[76,95] to highlight some of the features of deviational methods. We use the material properties of silicon, as described in Ref. 61. The mean free path $\Lambda = 388$ nm was calculated using

$$\Lambda = \frac{\sum_p \int V_g \tau D f^\mathrm{eq}_{T_\mathrm{eq}} d\omega}{\sum_p \int D f^\mathrm{eq}_{T_\mathrm{eq}} d\omega} \tag{76}$$

Figure 1 shows the steady-state temperature calculated for such a system, with $T_\mathrm{l} = 330$ K, $T_\mathrm{r} = 270$ K, for various values of Kn. Figure 2 shows the statistical uncertainty in the heat flux normalized by the local value of the heat flux (in this problem, the local value is constant across the domain), $\sigma_{\bar{q}''_x}/\bar{q}''_x$, for Kn $= 1$ as a function of the normalized temperature difference $|T_\mathrm{l} - T_\mathrm{r}|/T_0$. Specifically, we compare the statistical uncertainty of the variance-reduced case with $T_\mathrm{eq} = 300$ K to the nonvariance-reduced case for the silicon model (dispersion relation and relaxation times) described in Ref. 97, denoted as the frequency-dependent model, as well as for theoretical estimates corresponding to the gray Debye model of Section 3.5. Results for the formulation where each particle represents a fixed number of phonons and where each particle represents a fixed amount of energy are very close on the logarithmic scale and we therefore only show the latter. Figure 2 verifies that in the variance-reduced case, the standard deviation is proportional to the deviation $\Delta T = |T_\mathrm{l} - T_\mathrm{r}|$. For $\Delta T/T_\mathrm{eq} = 0.1$—which, for $T_\mathrm{eq} = 300$ K, corresponds to a relatively large amplitude of 30 K; the standard deviation is reduced by a factor of 7, meaning that the variance-reduced method can reach a given level of statistical uncertainty using $7^2 \approx 50$ times less samples. For $\Delta T/T_\mathrm{eq} = 0.01$, which corresponds to a temperature difference of 3 K, the speedup is approximately 5000 times. This is particularly important because it

is achieved without introducing any approximation, using algorithms of complexity that is comparable to the traditional methods discussed in Section 3.

5. SPATIALLY VARYING CONTROLS

In Section 4, we reviewed methods that use a simple class of functions as controls, namely, functions that are independent of time and space. On the other hand, Eq. (70) suggests that the amount of variance reduction increases as the control function approaches the nonequilibrium distribution. Methods that exploit this property by using a spatially dependent equilibrium designed to approximate the local equilibrium were originally developed for dilute gases.[67,82] Section 5 discusses a broader class of control functions that can be used to improve the efficiency but also the versatility of MC methods for simulating phonon transport.

Consider the following control function, $e^{\text{eq}}_{T_{\text{eq}}(\mathbf{x})}$, defined as a Bose-Einstein distribution with nonuniform temperature $T_{\text{eq}} = T_{\text{eq}}(\mathbf{x})$. The equation governing the deviation $e^{\text{d}} = e - e^{\text{eq}}_{T_{\text{eq}}(\mathbf{x})}$ can be written as follows:

$$\frac{\partial e^{\text{d}}}{\partial t} + \mathbf{V}_g \cdot \nabla_{\mathbf{x}} e^{\text{d}} = \frac{\left[e^{\text{loc}} - e^{\text{eq}}_{T_{\text{eq}}(\mathbf{x})}\right] - e^{\text{d}}}{\tau(\omega, p, T)} - \mathbf{V}_g \cdot \nabla_{\mathbf{x}} T_{\text{eq}} \frac{de^{\text{eq}}_{T_{\text{eq}}(\mathbf{x})}}{dT} \tag{77}$$

where the new "source term" on the right-hand side is a result of the fact that $e^{\text{eq}}_{T_{\text{eq}}}$ is no longer constant. As the name suggests, the term can be interpreted as a source of computational particles. Source terms arise in a number of contexts and are particularly useful in linear transport theory.[126,127] They will be discussed more in the context of linear problems in Section 6.

The total number of particles emitted by the source term in a time step Δt is given by

$$N_{\text{source}} = \frac{1}{\mathcal{E}^{\text{d}}_{\text{eff}}} \int \int \sum_p \frac{D}{4\pi} |\mathbf{V}_g \cdot \nabla_{\mathbf{x}} T_{\text{eq}}| \frac{de^{\text{eq}}_{T_{\text{eq}}(\mathbf{x})}}{dT} d^3\boldsymbol{\omega} d^3\mathbf{x} \Delta t \tag{78}$$

where the integration is performed over the whole domain. In addition to the above generation term, a spatially variable control requires the following changes compared to the constant control case described in Section 4.2:

1. The computational particles due to the source term must be generated from a distribution proportional to

$$-D(\omega, p)\mathbf{V}_g \cdot \nabla_{\mathbf{x}} T_{\text{eq}} \frac{de^{\text{eq}}_{T_{\text{eq}}(\mathbf{x})}}{dT} \tag{79}$$

A convenient way to ensure the proper distribution in space is to mix the approach based on a discretization of the cumulative distribution in frequency described in Section 3.1, and the acceptance-rejection method. Namely, one can first identify the maximum equilibrium temperature T_{max} and draw ω_0 and p_0 by numerically inverting the cumulative distribution taken at temperature T_{max}. The particle position $\mathbf{x}_0$ is then drawn uniformly and accepted if $\mathfrak{R} \leq (de^{\text{eq}}_{T_{\text{eq}}(\mathbf{x}_0)}/dT)/(de^{\text{eq}}_{T_{\text{max}}}/dT)$. In case of rejection, the process is repeated until a sample is accepted. The traveling

direction and the sign are then chosen from the angular distribution corresponding to $-\mathbf{V}_g \cdot \nabla_{\mathbf{x}} T_{\text{eq}}$. Because of the symmetry between positive and negative particles, simulations can be made more accurate by symmetrizing the emitted particles: if a positive particle is emitted at point $\mathbf{x}$ with properties (ω, p) and with direction $\mathbf{\Omega}$ (implying that $\mathbf{\Omega} \cdot \nabla_{\mathbf{x}} T_{\text{eq}} < 0$) a negative particle with the same properties is emitted in the symmetric direction $\mathbf{\Omega} - 2(\mathbf{\Omega} \cdot \hat{\mathbf{n}})\hat{\mathbf{n}}$, where $\hat{\mathbf{n}}$ is the normalized vector $\hat{\mathbf{n}} = \nabla_{\mathbf{x}} T_{\text{eq}} / \|\nabla_{\mathbf{x}} T_{\text{eq}}\|$. This process ensures that both the emitted heat flux and energy are zero. Although not essential, this contributes to reducing the statistical uncertainty.

2. Temperature (and pseudo-temperature) calculations in each cell need to account for the fact that the equilibrium energy density corresponding to the control function is spatially dependent. The heat flux due to $e^{\text{eq}}_{T_{\text{eq}}(\mathbf{x})}$ is zero, because the equilibrium distribution is isotropic in phase space.

3. Postscattering properties should be drawn from the distribution (75), accounting for the fact that T_{eq} is cell dependent. Although T_{eq} varies within cells, one can use the cell-average value, because the temperature T and pseudo-temperature $\tilde{T}$ are already (approximately) calculated based on cell-averaged properties. Drawing particle properties can again be achieved by combining the approach based on the inversion of the cumulative frequency distribution with the acceptance-rejection scheme.

Although a spatially variable control leads to a moderately more complex algorithm, it results in a number of benefits. In Section 5.1 we show how, when chosen suitably, a spatially variable control further reduces variance. This feature can be exploited for developing powerful multiscale simulation methods because it provides a means for focusing computational resources in regions where kinetic effects are important; this is further discussed in Section 7. In Section 6.6, we highlight a second benefit of this approach in connection with the simulation of externally applied temperature fields, which is of particular interest in the context of calculating the effective thermal conductivity of nanostructured materials.

5.1 Efficiency Gains in the Low-Knudsen Number Limit

The effect of a spatially variable control on the computational efficiency has been studied in more detail in the case of dilute gases, in which algorithms for spatially variable equilibrium with the objective of minimizing computational cost have been developed.[67,82] In these methods, the control is treated as piecewise constant in each cell and updated at the end of each time step, using a prescription that is designed[67,82] to enable the control to track the local equilibrium distribution.

Figure 4 shows a comparison of constant and variable-control methods in a dilute-gas analog of the problem described in Section 4.3, namely, heat exchange between two boundaries at different temperatures. Figure 4 compares the relative statistical uncertainty in the temperature measurement in a constant-control and variable-control simulation over the range $0.1 \leq \text{Kn} \leq 10$. The simulations (described in detail in Ref. 82) used $\sim$950 particles per cell. Figure 4 shows that as Kn decreases, the relative statistical uncertainty

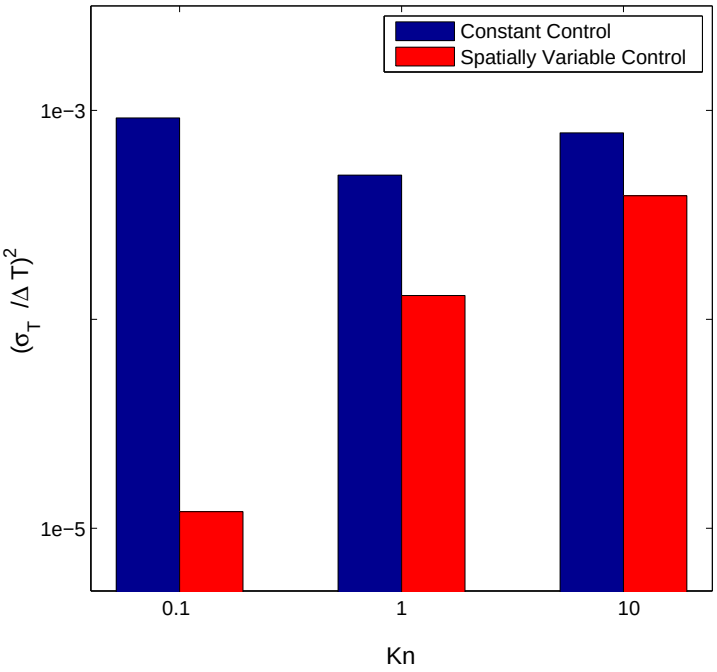

FIG. 4: For low Knudsen numbers, the relative statistical uncertainty is significantly reduced when a spatially variable equilibrium is used. From Ref. 82.

of the spatially variable control simulation decreases, leading to a variance reduction on the order of 50 as Kn goes from 10 to 0.1. This corresponds to a speedup on the order of 50. The reason for the improved performance is that as Kn decreases, the local equilibrium assumption becomes more appropriate (that is, as shown in Section 2.4, as $\mathrm{Kn} \to 0$, $f \to f^{\mathrm{loc}}$), ensuring that less particles are required to describe f, or for the same number of particles, lower variance is achieved.

This feature has important implications in the context of multiscale applications because it implies that such algorithms are able to focus the computational effort in regions where kinetic effects are important thus removing the stiffness associated with approaching the $\mathrm{Kn} \to 0$ limit with a Boltzmann solver.[82,128] This is further discussed in Section 7.

6. EFFICIENT METHODS FOR LINEARIZED PROBLEMS

In this section, we discuss a particularly efficient MC simulation method for solving the BTE in the relaxation-time approximation under linearized conditions. The computational benefits derive from combining the energy-based deviational formulation of Section 4.2, with two additional observations: first, for the small deviations from equilibrium encountered in practice, the governing BTE may be linearized with small error; second, in the relaxation-time approximation, modes (particles) are coupled only via the energy conservation statement (48).

By combining these ingredients, it is possible to show[64] that integration of the linearized Boltzmann equation can proceed with no need to calculate the temperature and pseudo-temperature; the latter is true because the linearized form of the energy conservation statement (48) is satisfied automatically in the energy-based formulation (by particle conservation). Particle trajectories are therefore no longer coupled (via the pseudo-temperature) and can be more efficiently simulated one at a time, using formulations that are reminiscent of neutron transport simulations.[126,129] In these formulations, no spatial or time discretization is used—in the form of cells and time step, respectively—leading to a simpler and more efficient simulation method that introduces no approximation (provided linearization is appropriate).

6.1 Linearized Boltzmann Equation in the Relaxation-Time Approximation

To derive the linearized Boltzmann equation we assume that the quantities $T - T_{\text{eq}}$ and $\tilde{T} - T_{\text{eq}}$ are comparable and small. We then use a Taylor expansion to write

$$\frac{D}{4\pi}\frac{e^{\text{eq}}_{\tilde{T}} - e^{\text{eq}}_{T_{\text{eq}}}}{\tau(T)} = \frac{D}{4\pi\tau(T_{\text{eq}})}\frac{de^{\text{eq}}_{T_{\text{eq}}}}{dT}(\tilde{T} - T_{\text{eq}}) + \mathcal{O}\left(\frac{\tilde{T} - T_{\text{eq}}}{T_{\text{eq}}}\right)^2 \tag{80}$$

where, for clarity, only the temperature dependence is made explicit.

The resulting linearized Boltzmann equation can be written as follows:

$$\frac{\partial e^{\text{d}}}{\partial t} + \mathbf{V}_g \cdot \nabla_{\mathbf{x}} e^{\text{d}} = \frac{\mathcal{L}(e^{\text{d}}) - e^{\text{d}}}{\tau(\omega, p, T_{eq})} \tag{81}$$

where

$$\mathcal{L}(e^{\text{d}})(\omega) = \frac{\int_{\omega'}\sum_{p'}(De^{\text{d}}/4\pi\tau)d^3\boldsymbol{\omega}'}{\int_{\omega'}\sum_{p'}(D/\tau)(de^{\text{eq}}_{T_{\text{eq}}}/dT)d\omega'}\frac{de^{\text{eq}}_{T_{\text{eq}}}}{dT}(\omega) \tag{82}$$

The last expression follows from the identity

$$(\tilde{T} - T_{\text{eq}})\int_{\omega}\sum_{p}\frac{de^{\text{eq}}_{T_{\text{eq}}}}{dT}\frac{D(\omega,p)}{\tau(\omega,p,T_{\text{eq}})}d\omega = \int_{\boldsymbol{\omega}}\sum_{p}\frac{D(\omega,p)e^{\text{d}}}{4\pi\tau(\omega,p,T_{\text{eq}})}d^3\boldsymbol{\omega} \tag{83}$$

which is the linearized form of Eq. (74).

Following the interpretation of Section 4.2, the linearized dynamics can be simulated by deleting particles according to the probability (47) with temperature T_{eq} and generating particles from the distribution

$$\frac{D}{4\pi\tau(T_{\text{eq}})}\frac{de^{\text{eq}}_{T_{\text{eq}}}}{dT}(\tilde{T} - T_{\text{eq}}) \tag{84}$$

Once normalized, this distribution does not depend on the pseudo-temperature or the temperature. Hence, at any time and at any location in the system, the properties of the scattered particles are drawn without knowledge of these two quantities; measuring them is therefore not necessary in this approximation, and discretization can be dispensed with, except for obtaining the desired estimates as outputs. Instead, particle trajectories can be simulated independently and, if the equilibrium temperature T_{eq} is constant in space and time, their motion can be simply simulated using a kinetic-Monte-Carlo-type algorithm[130] with a constant survival probability. This is discussed in more detail in Section 6.3.

6.2 Sources in Linear Transport Theory and the Superposition Principle

The linear formulation described above lends itself naturally to a number of powerful mathematical tools, such as superposition. In this section, we briefly describe how the idea of a source term, first introduced in Section 5, can be generalized to include terms resulting from initial and boundary conditions. Such formulations are very common in the formalism of linear transport theory,[126] where source terms are utilized to achieve additional variance reduction. In this review, we discuss generalized sources in the context of initializing simulations and simulating externally imposed temperature gradients. Examples of generalized source terms are given below.

Consider a system that is initially at temperature $T_{\text{i}}(\mathbf{x})$ in contact with an isothermal wall at temperature T_{w} at $x = 0$. This system can be modeled using the Boltzmann equation

$$\frac{\partial e^{\text{d}}}{\partial t} + \mathbf{V}_g \cdot \nabla_{\mathbf{x}} e^{\text{d}} = \frac{\mathcal{L}(e^{\text{d}}) - e^{\text{d}}}{\tau} + \sum_j Q_j \tag{85}$$

where $\sum_j Q_j = Q_i + Q_w$. The first term in the sum corresponds to the contribution of the initial condition and is given by $Q_i = \delta(t)(T_{\text{i}} - T_{\text{eq}}) de^{\text{eq}}_{T_{\text{eq}}}/dT$. The source resulting from the isothermal wall is given by $Q_w = \delta(x) H(\mathbf{V_g} \cdot \hat{\mathbf{n}})(\mathbf{V_g} \cdot \hat{\mathbf{n}})(T_{\text{w}} - T_{\text{eq}}) de^{\text{eq}}_{T_{\text{eq}}}/dT$. The Heaviside function specifies the direction of particle emission. The superposition principle allows one to solve for various subproblems using individual sources Q_j separately and to find the final answer by addition. This can be advantageous in a number of situations, for example, by allowing the number of particles used for each subproblem to be optimized separately.[126]

6.3 The Linearized Algorithm

Under the linearized formulation, particle trajectories are independent and particles can be simulated one at a time, which results in substantial memory savings. It also removes the burden of managing variable-size lists of particles because of particles leaving or entering the system.

Below, we describe the algorithm in the time-dependent case, with a fixed (in time and space) control temperature T_{eq}; we assume that we seek to calculate quantities such as the average temperature or heat flux in a given volume at times $\tilde{t}_1, \tilde{t}_2, ..., \tilde{t}_n$. Steady

problems can be treated more efficiently with a variant of this algorithm that does not require integration to steady state. This algorithm is discussed in Section 6.5.

Let the total deviational energy in the calculation due to n_s sources $Q_j,\ 1 \le j \le n_s$ be given by

$$E_{\text{tot}} = \int_\Gamma \frac{D}{4\pi} \sum_j |Q_j| d\Gamma = \sum_j |E_j| \tag{86}$$

where $\Gamma = (\mathbf{x}, \boldsymbol{\omega}, p, t)$ includes the "general phase-space coordinate" (which includes time and polarization). Given a desired number of simulation particles N_{part}, the effective deviational energy is determined by $\mathcal{E}^{\text{d}}_{\text{eff}} = E_{\text{tot}}/N_{\text{part}}$.

Individual particle trajectories are simulated as follows:

1. Draw the particle initial properties $\Gamma_0 = (x_0, y_0, z_0, \omega_0, \theta_0, \phi_0, p_0, t_0)$ from the appropriate source term as described in Section 3. The source from which the particle is to be generated is determined stochastically by noting that the probability of a particle originating from source k is given by $|E_k|/\sum_j |E_j|$.[64,131]

2. Calculate the time to the next scattering event $\Delta t = -\tau(\omega_0, p_0, T_{\text{eq}}) \ln(\mathfrak{R})$, where $\mathfrak{R}$ is a random number uniformly drawn in $(0, 1)$.

3. Define $\tilde{\mathbf{x}}_1 = \mathbf{x}_0 + \mathbf{V}_g \Delta t$. If the particle encounters a boundary along the line segment $(\mathbf{x}_0, \tilde{\mathbf{x}}_1]$, then set $\mathbf{x}_1$ to this encounter location and the time to the corresponding encounter time t_1. If no boundary interaction is detected, then set $\mathbf{x}_1 = \tilde{\mathbf{x}}_1$ and $t_1 = t_0 + \Delta t$.

4. Update the particle properties to $\omega_1, \theta_1, \phi_1, p_1$. If $\mathbf{x}_1$ is determined by collision with a boundary, then these properties are determined by the corresponding boundary condition. If $\mathbf{x}_1$ is determined by a relaxation event, then the new properties are drawn from the postscattering distribution

$$\frac{D(\omega, p)}{4\pi\tau(\omega, p, T_{\text{eq}})} \frac{de^{\text{eq}}_{T_{\text{eq}}}}{dT} \tag{87}$$

   Finally, the effective energy of the particle and the sign do not change over the complete trajectory. The energy-based formulation ensures that energy is conserved even when particles are considered individually.

5. Determine whether any of the measurement times $(\tilde{t}_1, ..., \tilde{t}_n)$ fall in the range $[t_0, t_1)$. If $\tilde{t}_i$ falls between t_0 and t_1, find the position of the particle at $t = \tilde{t}_i$ by interpolation. If the particle is located in the volume where the quantity of interest is calculated, then add the contribution of the particle to the average temperature in this volume at time $\tilde{t}_i$. For a total number N of simulated particles, the contribution to the energy from a particle with sign s is $s\mathcal{E}^{\text{d}}_{\text{eff}}$ and the contribution to the temperature is therefore $s\mathcal{E}^{\text{d}}_{\text{eff}}/(CV)$, where V is the volume of consideration and $C = \sum_p \int C_{\omega,p} d\omega$ is the heat capacity. The contribution to the heat flux at $\tilde{t}_i$ is then $s\mathcal{E}^{\text{d}}_{\text{eff}} \mathbf{V}_{g,0}/V$.

6. If $t_1 > \tilde{t}_n$, or if the particle is absorbed by a boundary, then the current particle trajectory is terminated. Otherwise, update $\Gamma_0 = \Gamma_1$ and return to step (2).

6.4 Domain of Validity

According to Eq. (80), the error committed by linearizing the Boltzmann equation is second order in the difference $T - T_{\text{eq}}$. Figure 5 shows a more quantitative measure of the discrepancy between the variance reduced [from Eq. (75)] and linearized [from Eq. (87)] gain term in the collision operator for silicon as a function of $T - T_{\text{eq}}$ for $T_{\text{eq}} = 300$ K, defined as

$$\epsilon = \left\{ \int_{\omega} \sum_{p} \hbar\omega \left| \frac{D}{\tau(\omega, p, T)} \left[\frac{1}{\exp\left(\hbar\omega / k_{\text{B}} T\right) - 1} - \frac{1}{\exp\left(\hbar\omega / k_{\text{B}} T_{\text{eq}}\right) - 1} \right] \right.\right.$$
$$\left.\left. - (T - T_{\text{eq}}) \frac{D}{\tau(\omega, p, T_{\text{eq}})} \frac{de^{\text{eq}}_{T_{\text{eq}}}}{dT} \right| d\omega \right\} \Bigg/ \left[\int_{\omega} \sum_{p} \frac{\hbar\omega D}{\tau(\exp\left(\hbar\omega / k_B T_{\text{eq}}\right) - 1)} d\omega \right] \quad (88)$$

Figure 5 verifies that the error is second order in $T - T_{\text{eq}}$. This analysis suggests that the error is still acceptable (<3%) up to temperature differences on the order of 30 K.

Here we note that according to this analysis, quantities such as temperature or heat flux in the linear approximation are accurate to the second order in ΔT. The effective thermal

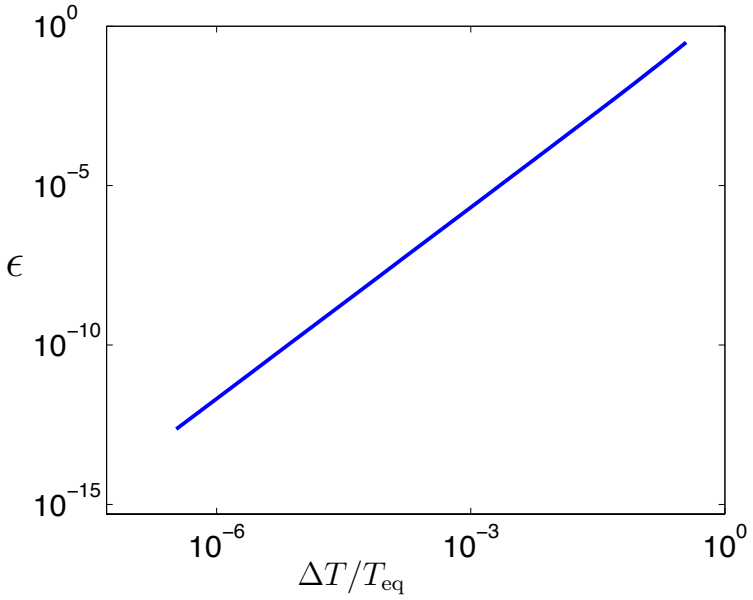

FIG. 5: Normalized error between the linearized and exact collision operator, in the case where $T_{\text{eq}} = 300$ K. For $\Delta T / T_{\text{eq}} = 0.1$, i.e., for a temperature difference $\Delta T = 30$ K, the relative error, ϵ, is $\sim$2.2%.

conductivity, however, is first-order accurate because it is calculated by dividing the heat flux by a quantity proportional to ΔT.

Because the accuracy of the method is directly related to $T - T_{\text{eq}}$, it could be improved by choosing a spatially variable control. This however would require a significantly more complex simulation algorithm because it would lead to trajectory-dependent relaxation times.

6.5 Steady-State Formulations

Particle simulation methods are inherently explicit in time. Therefore, even steady problems are solved by integrating to the steady state and then sampled by extending the time integration further. Recent work[95] on simulation methods that arrive to the steady solution without explicit integration to it required the introduction of iteration as well as approximations (see Section 6.6.1, for more details). An alternative approach based on the Wild sum has also been pursued,[132,133] but has been limited to simple models and required the use of approximations.

The linearized algorithm discussed above lends itself naturally to the simulation of steady-state solutions directly and without integrating to steady state first, primarily because individual particle trajectories are decoupled. Such steady-state formulations and the associated class of steady-state estimators that record continuously[126] over the particles trajectories are presented here as extensions of the time-dependent case. Alternative (more mathematical) developments of the methodology for treating steady-state problems directly can be found in the linear transport theory literature (see, for example, Ref. 126).

In transient problems, quantities of interest at time t can be written as follows:

$$A_g(t) = \int_{\mathbf{x}} \int_{\boldsymbol{\omega}} \sum_p g \frac{De^{\text{d}}}{4\pi} d^3\boldsymbol{\omega} d^3\mathbf{x} \tag{89}$$

where e^{d} is taken at time t and both the integration bounds and function g depend on the quantity of interest. For instance, in the case of the average heat flux in a volume V, g is the vector $\mathbf{V}_g/V$. As in Section 3.5, replacing $De^{\text{d}}/(4\pi)$ by its particle approximation yields

$$\bar{A}_g(t) = \mathcal{E}^{\text{d}}_{\text{eff}} \sum_{i=1}^{N_{\text{part}}} s_i g[\mathbf{x}_i(t), \boldsymbol{\omega}_i(t), p_i(t)] \tag{90}$$

The steady-state case can be motivated by introducing time averaging

$$\bar{A}_g(ss) = \frac{1}{\mathcal{T}} \int_{t'=t_{ss}}^{t_{ss}+\mathcal{T}} \bar{A}_g(t')dt' \tag{91}$$

over a time period $\mathcal{T}$, after time t_{ss} has passed deemed sufficient for steady conditions to prevail. This results in the estimator

$$\bar{A}_g(ss) = \frac{\mathcal{E}^{\mathrm{d}}_{\mathrm{eff}}}{\mathcal{T}} \sum_{i=1}^{N_{\mathrm{part}}} s_i \int_{t'=\max(t_i^{\mathrm{start}}, t_{ss})}^{t_{ss}+\mathcal{T}} g(\mathbf{x}_i(t'), \boldsymbol{\omega}_i(t'), p_i(t'))dt' \tag{92}$$

where t_i^{start} is the time at which particle i is emitted.

Here we note that for a steady-state (time-independent) solution to exist, all sources must be time independent. Hence, the definition of the total deviational energy rate follows from Eq. (86)

$$\dot{E}_{\mathrm{tot}} = \frac{E_{\mathrm{tot}}}{(t_{ss}+\mathcal{T})} = \int_{\mathbf{x}} \int_{\boldsymbol{\omega}} \frac{D}{4\pi} |Q| d^3\boldsymbol{\omega} d^3\mathbf{x} \tag{93}$$

where, here, $Q = \sum Q_j$ denotes all steady particle sources.

Let us examine now what happens if, instead of terminating the particle trajectories at $t = t_{ss} + \mathcal{T}$, we keep track of them indefinitely until they exit the simulation, which will usually happen through an absorbing boundary (e.g., isothermal wall). This amounts to letting $\mathcal{T} \to \infty$, which has two implications. First, the expected number of particles emitted before $t = t_{ss}$ is negligible, which implies that all particle contributions to the quantity of interest are recorded over their complete trajectory, from emission to exit or termination; in other words, the time interval $0 \le t \le t_{ss}$ need not be explicitly simulated. Second, the expression of the estimate (92) tends to

$$\bar{A}_g(ss) = \sum_{i=1}^{N_{\mathrm{part}}} \dot{\mathcal{E}}^{\mathrm{d}}_{\mathrm{eff}} \int_{t'=t_i^{\mathrm{start}}}^{t_i^{\mathrm{end}}} g(\mathbf{x}_i(t'), \boldsymbol{\omega}_i(t'), p_i(t'))dt' \tag{94}$$

where t_i^{end} is the exit or termination time for a given particle i. The particle contribution is therefore a curvilinear integral over the whole trajectory. Estimators such as (94) are typically referred to as *track length estimators*. We note that the effective deviational energy is now replaced by the effective deviational energy rate $\dot{\mathcal{E}}^{\mathrm{d}}_{\mathrm{eff}} \equiv \dot{E}_{\mathrm{tot}}/N_{\mathrm{part}}$, which results from the removal of the time dimension.

In Section 6.6, we will be interested in the average heat flux over the whole simulation domain in the direction of an applied temperature gradient $\hat{\mathbf{n}} = -\nabla_{\mathbf{x}} T / \|\nabla_{\mathbf{x}} T\|$. Let us consider this case as an illustration of the above development. The quantity of interest can be written as

$$q''_{\hat{\mathbf{n}}} = \frac{1}{V} \int_{\mathbf{x}} \int_{\boldsymbol{\omega}} \mathbf{V}_g \cdot \hat{\mathbf{n}} \frac{De^{\mathrm{d}}}{4\pi} d^3\boldsymbol{\omega} d^3\mathbf{x} \tag{95}$$

allowing us to identify the individual particle contribution as

$$q''_{\hat{\mathbf{n}},i} = \frac{\dot{\mathcal{E}}^{\mathrm{d}}_{\mathrm{eff}}}{V} \int_{\mathrm{path}} \mathbf{V}_g \cdot \hat{\mathbf{n}} dt \tag{96}$$

For the time interval $t_0 \le t \le t_f$ in which the particle travels from $\mathbf{x}_0$ to $\mathbf{x}_f$

$$\int_{t=t_0}^{t_f} \mathbf{V}_g \cdot \hat{\mathbf{n}} dt = (\mathbf{x}_f - \mathbf{x}_0) \cdot \hat{\mathbf{n}} \tag{97}$$

We note that the time coordinate, formally used for the purpose of the derivation, is not present in the final expression.

6.6 Application: Thermal Conductivity of Periodic Nanostructures

The linearized formulation described in Section 6 is particularly suited to the calculation of the effective thermal conductivity of periodic nanostructures, which are inherently low temperature-difference, steady-state simulations. In this section, we describe how such calculations can be performed using a spatially variable equilibrium to simulate an "imposed temperature gradient." The discussion that follows refers to Fig. 6, which shows the unit cell of a chosen periodic nanostructure.

We assume that we seek to calculate the effective thermal conductivity in the direction $\hat{\mathbf{n}}$. This is achieved by applying a macroscopic temperature gradient $\nabla_{\mathbf{x}} T$ in this direction and calculating the resulting average heat flux. Because the temperature gradient is not constant inside a unit cell, the notion of an imposed temperature gradient needs to be understood as the overall temperature gradient perceived at length scales large compared to the size of the unit cell.[100] We also assume that the temperature gradient applied is small, because a large temperature gradient would result in a nonlinear response which is undesirable (in the definition of the thermal conductivity).

Here we start our discussion by reviewing the approach of Hao et al.,[28] which states that, referring to points $\mathbf{x}_1$ and $\mathbf{x}_2$ in Fig. 6, the deviation from equilibrium is periodic [see Eq. (68)], leading to

$$e_1^{\text{in}} - e_{T_1}^{\text{eq}} = e_2^{\text{out}} - e_{T_2}^{\text{eq}} \tag{98}$$

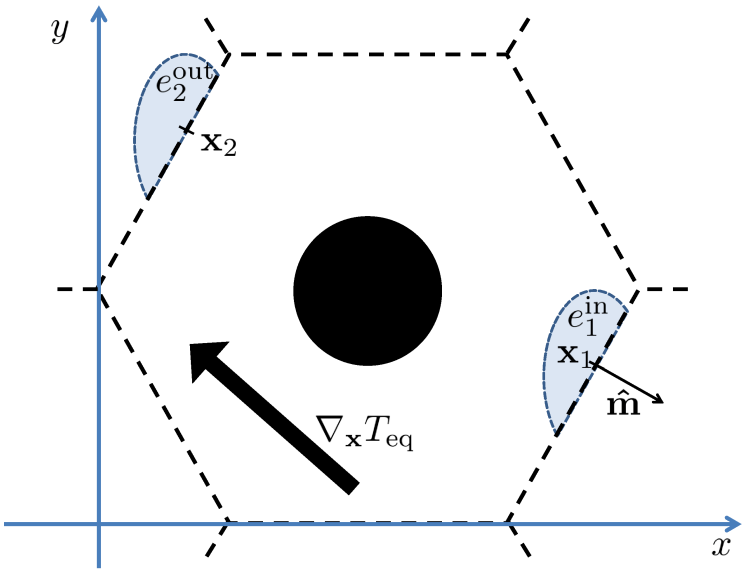

FIG. 6: Example of periodic nanostructure with hexagonal symmetry. The cylindrical pores are assumed to be diffusely reflecting.

$$e_2^{\text{in}} - e_{T_2}^{\text{eq}} = e_1^{\text{out}} - e_{T_1}^{\text{eq}} \tag{99}$$

where $e_{1,2}^{\text{in}}$ (respectively, $e_{1,2}^{\text{out}}$) refers to the distribution entering (respectively, exiting) the cell, such that $\mathbf{\Omega} \cdot \hat{\mathbf{m}} < 0$ (respectively, $\mathbf{\Omega} \cdot \hat{\mathbf{m}} > 0$), where $\hat{\mathbf{m}}$ is, as shown in Fig. 6, the outward-pointing normal. The difference between T_1 and T_2 results from the applied macroscopic thermal gradient.

In the case of a fixed control equilibrium, we can write these boundary conditions in the deviational form

$$e_1^{\text{in}} - e_{T_{\text{eq}}}^{\text{eq}} = e_2^{\text{out}} - e_{T_{\text{eq}}}^{\text{eq}} + e_{T_1}^{\text{eq}} - e_{T_2}^{\text{eq}} \tag{100}$$

$$e_2^{\text{in}} - e_{T_{\text{eq}}}^{\text{eq}} = e_1^{\text{out}} - e_{T_{\text{eq}}}^{\text{eq}} + e_{T_2}^{\text{eq}} - e_{T_1}^{\text{eq}} \tag{101}$$

Given these expressions, the deviational approach with fixed equilibrium amounts to emitting particles at the periodic boundaries from the distributions $e_{T_1}^{\text{eq}} - e_{T_2}^{\text{eq}}$ or $e_{T_2}^{\text{eq}} - e_{T_1}^{\text{eq}}$, respectively. The trajectories of these particles are then computed following the standard algorithm, subject to periodic boundary conditions appropriate to the unit cell simulated. In the general case, such as the one shown in Fig. 6, the values of T_1 and T_2 can vary along the boundaries, making generation of particles from these surface sources cumbersome.

An alternative approach consists of using a spatially variable equilibrium (control). As shown in Section 5, a spatially variable equilibrium requires volumetric generation of particles from the source

$$Q_s = -\mathbf{V}_g \cdot \nabla_{\mathbf{x}} T_{\text{eq}} \frac{de_{T_{\text{eq}}}^{\text{eq}}}{dT}. \tag{102}$$

Despite this, it is the preferable approach because it results in a simpler overall algorithm. To show this, we linearize the boundary conditions (101) about T_0, the temperature at which we calculate the thermal conductivity, to obtain

$$e_1^{\text{in}} - e_{T_0}^{\text{eq}} = e_2^{\text{out}} - e_{T_0}^{\text{eq}} + \frac{de_{T_0}^{\text{eq}}}{dT}(T_1 - T_2) \tag{103}$$

$$e_2^{\text{in}} - e_{T_0}^{\text{eq}} = e_1^{\text{out}} - e_{T_0}^{\text{eq}} + \frac{de_{T_0}^{\text{eq}}}{dT}(T_2 - T_1) \tag{104}$$

which, using $T_{\text{eq}}(\mathbf{x}) = T_0 + \mathbf{x} \cdot \nabla_{\mathbf{x}} T_{\text{eq}}$, becomes

$$e_1^{\text{in}} - e_{T_0}^{\text{eq}} = e_2^{\text{out}} - e_{T_0}^{\text{eq}} + \frac{de_{T_0}^{\text{eq}}}{dT} \nabla_{\mathbf{x}} T_{\text{eq}} \cdot (\mathbf{x}_1 - \mathbf{x}_2) \tag{105}$$

$$e_2^{\text{in}} - e_{T_0}^{\text{eq}} = e_1^{\text{out}} - e_{T_0}^{\text{eq}} + \frac{de_{T_0}^{\text{eq}}}{dT} \nabla_{\mathbf{x}} T_{\text{eq}} \cdot (\mathbf{x}_2 - \mathbf{x}_1) \tag{106}$$

Finally, noting that the control function, under linearized conditions, is $e_{T_0}^{\text{eq}} + \mathbf{x} \cdot \nabla_{\mathbf{x}} T_{\text{eq}} de_{T_0}^{\text{eq}} / dT$, we can write

$$e_1^{\text{in,d}} = e_2^{\text{out,d}} \tag{107}$$

$$e_2^{\text{in,d}} = e_1^{\text{out,d}} \tag{108}$$

In other words, the requirement of periodic deviation from local equilibrium (68) can be achieved using a spatially variable control to impose the temperature gradient, while subjecting the deviational particle population to periodic boundary conditions. Although the two approaches are equivalent, the latter is arguably simpler, more efficient, and allows one to conveniently calculate the thermal conductivity in an arbitrary direction. We also remark that the latter formulation directly follows from a homogenization approach,[101] treating the ratio of the unit cell size to the length scale of the externally imposed temperature gradient as a small parameter.

Because of the steady-state nature of the problem sketched in Fig. 6, and due to its reduction to a 2D problem in physical space, the computational particles represent here a deviational energy per unit time and per unit length given by

$$\dot{\mathcal{E}}^{\mathrm{d}}_{\mathrm{eff}} = \frac{1}{N_{\mathrm{part}}} \int\int \sum_p \nabla_{\mathbf{x}} T_{\mathrm{eq}} \cdot \mathbf{V}_g \frac{D}{4\pi} \frac{de^{\mathrm{eq}}_{T_{\mathrm{eq}}}}{dT} d^3\boldsymbol{\omega} d^2\mathbf{x} \tag{109}$$

where the integration in space is performed over a unit cell of the periodic structure. Moreover, using steady-state sampling means that the heat flux along the temperature gradient can be evaluated over the whole unit cell using

$$q''_{\hat{\mathbf{n}}} = \frac{1}{\mathcal{A}} \int\int e^{\mathrm{d}} \frac{D}{4\pi} \mathbf{V}_g \cdot \hat{\mathbf{n}} d^3\boldsymbol{\omega} d^2\mathbf{x} \tag{110}$$

where $\mathcal{A}$ is understood here as the area of the unit cell. In three dimensions, this is replaced by the cell volume. The simulations otherwise proceed as outlined in Sections 6.3 and 6.5, with the addition of a mechanism for terminating particle trajectories, which is necessary because of the steady-state formulation and the type of boundary conditions used here; this is discussed in detail in Section 6.6.1. Regarding boundary conditions, any particle leaving the cell is reinserted through the corresponding periodic side. For instance, in Fig. 6, a particle exiting the cell at point $\mathbf{x}_1$ would reenter at $\mathbf{x}_2$.

6.6.1 Termination of Particle Trajectories

In a number of practical cases, particle trajectories terminate when the particle exits the system, usually through an absorbing boundary (isothermal wall). In periodic nanostructures, this cannot happen due to the periodic boundary conditions; therefore other termination criteria must be developed. In Ref. 64, it was observed that the average contribution of particles to the heat flux monotonically decreases in absolute value along the particle's trajectory (with the number of scattering events). It was therefore proposed that a particle trajectory can be terminated when its contribution to the heat flux reaches the order of magnitude of the statistical uncertainty associated with each trajectory segment. This was empirically determined to correspond to a number of scattering events, N_s, on the order of 50.[64] Estimates of the heat flux field resulting from this method are shown in Fig. 7.

In their steady-state formulation, Randrianalisoa and Baillis[95] proposed an approach for imposing energy conservation that can be adapted here for terminating the particle trajectories, at the expense of introducing discretization in space. We illustrate this approach with the following example: we consider a periodic nanostructure composed of parallel,

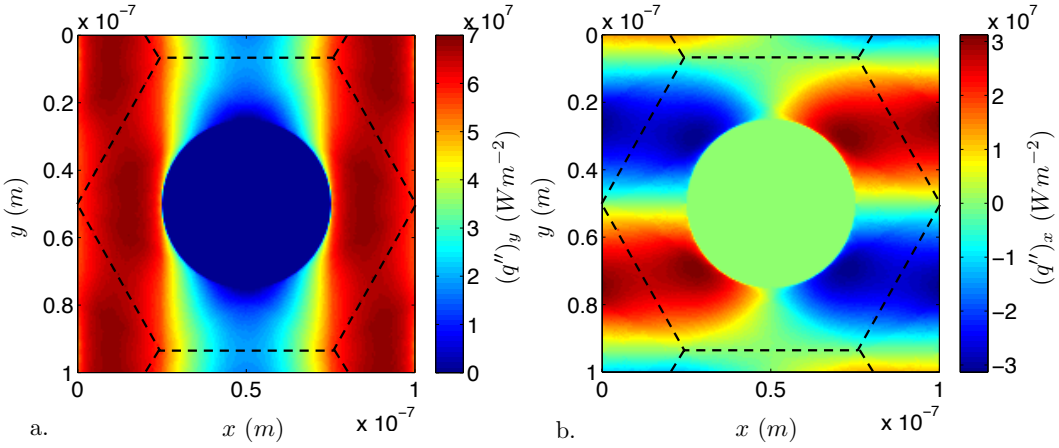

FIG. 7: x and y components of the heat flux in the elementary cell of a triangular network of cylindrical pores subjected to a temperature gradient of 10^6 K m^{-1} in the y-direction. The pore surfaces are assumed diffusely reflective.

adiabatic (diffusely reflective) plane surfaces normal to the applied temperature gradient; the spacing between the surfaces is d = 100 nm (see Fig. 8). This example was chosen because the effective thermal conductivity of this structure is exactly known ($\kappa_{\text{eff}} = 0$). This allows us to investigate the error associated with the discretization in space introduced by this method but also more easily illustrate the theoretical concept on which this algorithm is based.

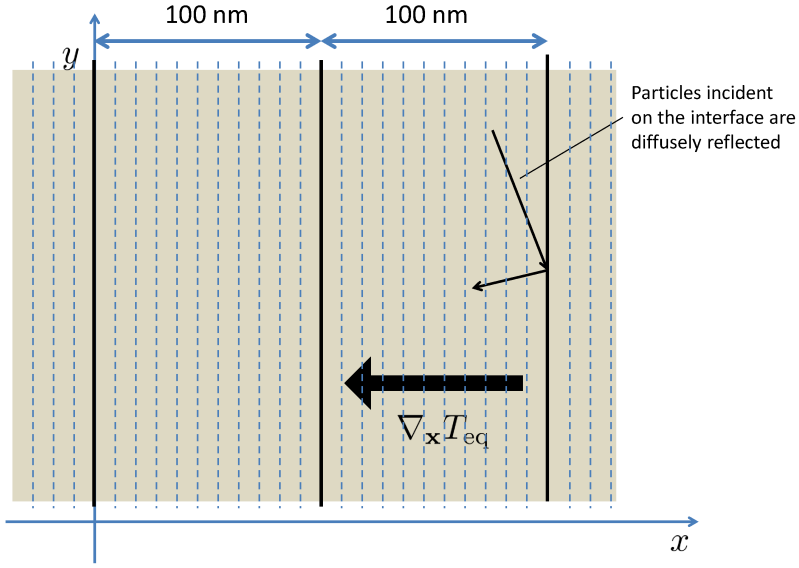

FIG. 8: Fictitious material with diffusely reflective interfaces normal to the direction of the applied temperature gradient. Dashed lines denote the cell grid used to calculate $\psi_j(x)$, defined in Section 6.6.1.

The simulation proceeds in general terms as described in Section 6.3, but with one major difference. Instead of simulating each particle to the end of their trajectory, each particle is simulated until its first relaxation event. At this time, the local density of energy "loss" events

$$\psi_1 = \frac{1}{\Delta x} \int_{x \in \text{cell}} \int_{\boldsymbol{\omega}} \frac{D e_1^{\text{d}}}{4\pi\tau} d^3\boldsymbol{\omega} dx \tag{111}$$

is calculated by recording the number of trajectories terminating at each of the computational cells of length Δx in which the domain is discretized. For this a cell-grid is used that is similar to the one in the cell-based algorithms described in Sections 3 and 4; for the particular one-dimensional problem discussed here, the cell-grid is shown in Fig. 8.

Energy conservation requires that energy relaxation events are followed by the emission of new computational particles from the "gain" term of the Boltzmann equation, $\mathcal{L}(e_1^{\text{d}})/\tau$. The number of these particles is determined from energy conservation, which requires their number be such that they carry the same amount of energy as the net energy carried by particles whose trajectories have been terminated. The intermediate step of advancing all particles up to their first scattering event coupled with the observation that the net amount of energy needs to be conserved, allows cancellation between positive and negative particles within the same cell to take place, as was utilized before in the time step-based algorithm of Section 4.

Following this cancellation, the algorithm can proceed by noting that integration of the particle trajectories up to the first relaxation event corresponds to solution of the equation

$$\mathbf{V}_g \cdot \nabla_{\mathbf{x}} e_1^{\text{d}} = -\frac{e_1^{\text{d}}}{\tau} + Q_s \tag{112}$$

while ψ_1 is a register of the amount of particles to be generated in each cell from $D\mathcal{L}(e_1^{\text{d}})/\tau$. This information can now be used for solving

$$\mathbf{V}_g \cdot \nabla_{\mathbf{x}} e_2^{\text{d}} = -\frac{e_2^{\text{d}}}{\tau} + \frac{\mathcal{L}(e_1^{\text{d}})}{\tau} \tag{113}$$

where the new source term $\mathcal{L}(e_1^{\text{d}})/\tau$ is approximated by generating $\psi_1 \Delta x / \dot{\mathcal{E}}_{\text{eff}}^{\text{d}}$ particles whose frequencies and polarizations are drawn from the postscattering distribution $D\mathcal{L}(e_1^{\text{d}})(\omega, p)/\tau(\omega, p, T_{\text{eq}})$. Here, $\dot{\mathcal{E}}_{\text{eff}}^{\text{d}}$ is the particle effective energy rate per unit area. The starting position for each particle is uniformly drawn within the given cell, and the traveling direction is isotropically chosen because the postscattering distribution is isotropic in this model.

The process is repeated until the number of particles emitted by the new sources is 0, that is, until complete cancellation has been achieved. The latter is guaranteed by the fact that the net energy rate emitted by the initial source is 0 (the same number of positive and negative particles are involved in the simulation). (If this was not the case, i.e., if a nonzero energy rate was emitted, the problem would be ill-posed because a steady state could not exist without absorbing boundaries.)

This approach can now be explained by noting that it corresponds to the decomposition $e^{\text{d}} = e_1^{\text{d}} + e_2^{\text{d}} + ...$, where step $j > 1$ in the above process solves the equation

$$\mathbf{V}_g \cdot \nabla_{\mathbf{x}} e_j^{\mathrm{d}} = -\frac{e_j^{\mathrm{d}}}{\tau} + \frac{\mathcal{L}(e_{j-1}^{\mathrm{d}})}{\tau} \tag{114}$$

At each level, the number of particles to be generated from the source term $D\mathcal{L}(e_j^{\mathrm{d}})/\tau$ is given by ψ_j. Step $j = 1$ corresponds to Eq. (112). Summing over all j recovers the linearized Boltzmann transport equation

$$\mathbf{V}_g \cdot \nabla_{\mathbf{x}} e^{\mathrm{d}} = \frac{\mathcal{L}(e^{\mathrm{d}}) - e^{\mathrm{d}}}{\tau} + Q_s \tag{115}$$

From the above, it follows that the track length estimator needs to be applied to each segment of trajectory in order to calculate the corresponding heat flux contributions. Figure 9(a) shows the distribution of ψ and heat flux corresponding to various steps in the process for the problem considered here. In this particular example, the heat flux at any level j [Fig. 9(b)] is nonzero. However, the combined contribution of all steps results in a zero heat flux (within the numerical approximation), as expected.

The latter observation is used here to investigate the numerical error associated with the introduction of a grid for the calculation of the source terms ψ_j. Figure 10 shows the difference between the numerical value of the heat flux and the exact result as a function of the cell size (Δx). The results show that the discretization error is of second order in Δx, in analogy with the second-order accuracy observed[70,71,74] in DSMC algorithms. Extension to 2D and 3D cases is straightforward.

In summary, while the cancellation approach outlined here is not needed in cases where particle trajectories are made finite due to the existence of absorbing boundaries, combining it with the linearized and variance-reduced approach can benefit the case of periodic nanostructures where absorbing boundaries may not be present. Figure 11 shows that the number of particles decreases exponentially as a function of j. This results in an appreciable speedup (factor of around 10) with respect to the approach based on an empirical choice of the termination criterion,[64] at the expense of a second-order approximation in Δx and a slightly more complicated algorithm.

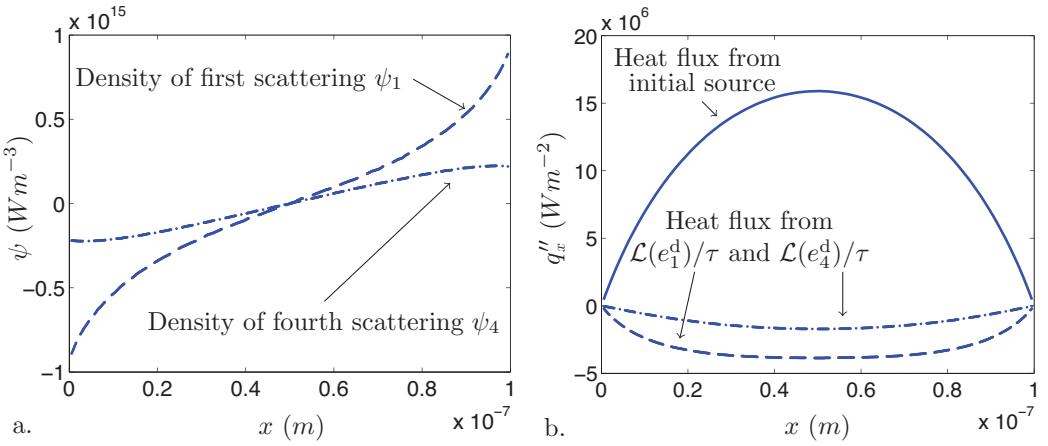

FIG. 9: (a) ψ_1 and ψ_4 and (b) heat flux contributions resulting from Q_s, $\mathcal{L}(e_1^{\mathrm{d}})/\tau$ and $\mathcal{L}(e_4^{\mathrm{d}})/\tau$. These results were obtained using an imposed temperature gradient of 10^6 K m^{-1}.

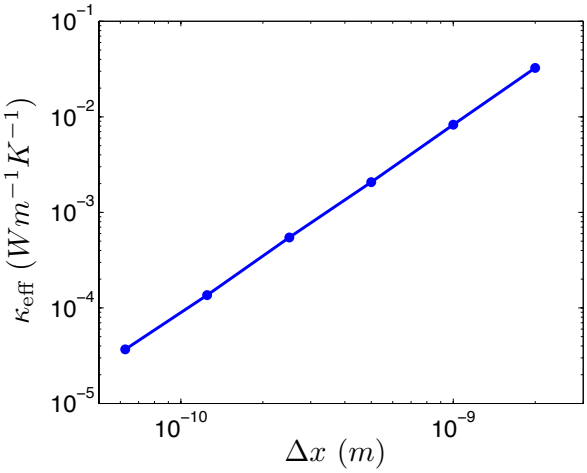

FIG. 10: Error in the effective thermal conductivity of the structure in Fig. 8 as a function of the cell-grid size Δx. The convergence order is quadratic.

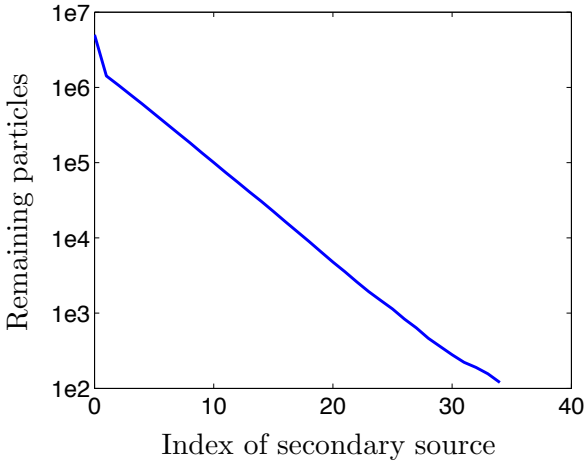

FIG. 11: Using the termination technique based on spatial discretization, the number of particles in the system decreases exponentially.

6.6.2 Final Remarks

Here we note that the linearized algorithm owes much of its simplicity to the fact that the particle survival probability is constant. When temperature changes across the domain are large, the relaxation time is no longer constant along particle trajectories making prediction of the next relaxation event path dependent and, as a result, significantly more complex. This appears to have been neglected in Ref. 95.

Finally, we also note that the example of Fig. 8 provides another illustration of the fact that, as detailed in Section 2.4, calculating the effective thermal conductivity based on the

mean free path including boundary scattering is in general incorrect. The effective thermal conductivity of the structure shown in Fig. 8 is nonisotropic and zero in the direction normal to the diffuse interfaces. On the other hand, the average distance a particle travels between relaxation events or collisions with an interface is clearly finite, thus yielding the wrong estimate for the effective thermal conductivity if used in the first term of Eq. (23).

6.7 Computational Efficiency

The benefits associated with the linearized formulation are numerous, provided linearization of the governing equation is justified. In addition to being significantly easier to code, the linearized simulation is significantly more efficient because it involves less operations per simulated particle and uses significantly less memory. Of particular note is its ability to avoid the stiffness associated with disparate relaxation times because it allows each particle to evolve at its own characteristic time, rather than requiring a time step that is much smaller than the smallest relaxation time.

Clearly, the speedup compared to other methods will be problem dependent because it will depend on a number of factors, such as the ratio of the largest to the smallest relaxation time. It was reported in Ref. 64 that over a number of applications, the speedup ranged between a factor of 100 and 1000. Figure 12 shows a comparison between two simulations of a transient thermoreflectance (TTR) experiment[61] using the deviational algorithm of Section 4.2 and the linearized algorithm described in Section 6. More details on the problem formulation can be found in Ref. 61. Figure 12 shows that for (approximately) the same computational cost, the linearized algorithm can reach simulation times up to 10 μs, which is approximately three orders of magnitude longer than the other deviational method.

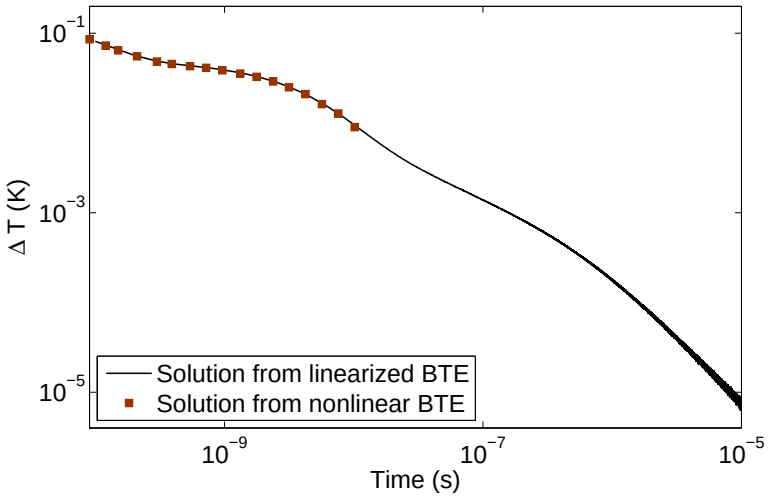

FIG. 12: Surface temperature in simulation of a TTR experiment as a function of time, calculated with the variance-reduced Monte Carlo method using time steps,[61] and the linearized method presented in Ref 64 and 131. The latter reaches significantly longer times.

Similar speedups have been observed in calculations of nanostructured materials. Specifically, a highly resolved (results reported on a 50×50 grid) simulation of the 2D nanostructure discussed in Section 6.6, using the silicon material model discussed in Ref. 61, and featuring 25×10^6 simulation particles ($N_s = 40$) and 1000 points to discretize the dispersion relation, requires $\sim$30 min on a single core of an Intel I-7 processor. On the other hand, an estimate for the effective thermal conductivity, which does not require spatial resolution of the temperature field, requires only 1 min of run time because all particles contribute toward the heat flux estimate. For this reason, we expect that the simulation of three-dimensional geometries will not result in a large increase in computational cost.

The above examples show that the linear method discussed in this section has the potential to play an important role in interpreting experimental investigations of phonon transport because it lends itself naturally to problems which require variable/adaptive resolution (e.g., transient thermoreflectance[40,41]), by using more computational particles where the deviation from equilibrium is large and less particles in regions where the solution can be described analytically.

In some cases, additional speedup may be possible by exploiting the duality between the Boltzmann equation and its adjoint, using techniques already developed in the fields of neutron and photon transport, and more generally in linear transport theory.[126,134] In the case of phonon transport, it can be shown[135] that in cases where a signal detector is small but the signal source is large, that is when the signal is only needed in some small spatial or spectral region, significant computational savings can be achieved by solving the adjoint Boltzmann equation

$$-\frac{\partial e^*}{\partial t} - \mathbf{V}_g \cdot \nabla_{\mathbf{x}} e^* = \frac{\mathcal{L}(e^*) - e^*}{\tau} + g \tag{116}$$

In Eq. (116) particles simulating the adjoint solution e^* evolve backward in time and are emitted by the source g, which is related to the detector in the original problem. Conversely, computational particles are collected by a detector that is related to the source in the original problem. Because of the large difference in size between the source and detector in the original problem, the adjoint formulation ensures that the signal collected by the detector will be significantly enhanced leading to improved variance reduction.

7. MULTISCALE PROBLEMS

Computational methods that can efficiently but also accurately model problems exhibiting a wide range of length and time scales remain highly desirable and the subject of considerable research effort.

The first attempts for addressing this need in the field of kinetic transport appeared more than two decades ago,[136] in the form of hybrid methods. These methods aim to minimize the computational cost by using the kinetic description (e.g., MC simulation) only in regions where it is needed, while the remainder of the computational domain is treated by the less expensive NSF description. The literature on such methods is quite extensive, with the majority of methods addressing the dilute-gas problem. Our discussion here will briefly review the basic ideas behind these methods from the point of view of

phonon-mediated heat transport. The hybrid formulations described above typically employ domain decomposition techniques[137] to separate the two regions in question. As a result, appropriate information exchange between the two descriptions becomes central to the success of the method.[138] Fortunately, a recipe for information exchange is readily available in kinetic transport problems: the CE expansion, briefly discussed in Section 2.4, provides an analytical description of the distribution function in the limit $\mathrm{Kn} \to 0$.[9,11,59] This distribution, parameterized by the local values of the NSF solution field at the coupling boundary, can be used as a rigorous boundary condition for the kinetic (BTE) solver. Methods for generating the CE expansion have also been developed.[139] Transitioning from the kinetic solver to the NSF description is simple because this corresponds to a process of averaging (moment evaluation). The existence of CE theory has led to the development of fairly sophisticated hybrid simulation methods[140–142] in which the transition from one description to the other is automatic and, in some cases, seamlessly integrated within a mesh refinement process. Criteria for transition from one description to the other have also been investigated.[140,143]

These methods assume that the region where kinetic effects are important is sufficiently localized and small that the kinetic part of the calculation is feasible. For a large class of problems of practical interest, this is not the case. As discussed in more detail in Ref. 128, the deviational methods described in Section 4 can be thought of as multiscale methods that utilize algebraic decomposition of the distribution function into an equilibrium part and the deviation therefrom to more efficiently simulate multiscale problems. By separating out the (large) part that can be described by an equilibrium distribution, the number of particles needed to describe the phenomenon of interest is reduced drastically, or alternatively, focused on the regions where kinetic effects are appreciable. In other words, these algorithms automatically and adaptively focus computational resources where kinetic effects are important. An example is the simulation of the TTR experiment discussed in Section 4: as a result of the localized heating, large parts of the computational domain are in thermal equilibrium, especially for early times. Algebraic decomposition enables the use of particles only in regions where $e^{\mathrm{d}} \neq 0$, thus significantly reducing the computational cost compared to traditional approaches, which would need to fill the whole computational domain with computational particles, the vast majority of which would be reproducing, albeit noisily, an equilibrium distribution.

In the above context, deviational methods using a spatially variable equilibrium distribution are even more powerful because they can use a control that captures locally varying equilibrium conditions. Specifically, as shown by Eq. (20), local equilibrium corresponds to the leading order term in the Chapman-Enskog expansion, with deviations therefrom (requiring particles for their description) scaling as O(Kn) or higher. Thus, in contrast to standard particle simulation methods that become increasingly more expensive as the NSF ($\mathrm{Kn} \to 0$) limit is approached (larger length scales imply not only more simulation particles, but also longer evolution time scales), deviational methods with a spatially variable equilibrium distribution become more efficient as this limit is approached because they are able to relegate increasingly more of the description to the equilibrium part, thus reducing the number of particles required for the simulation.[128] Such methods have been developed for dilutes gases[67,82] and shown to exhibit enhanced variance reduction, particularly as

$\mathrm{Kn} \to 0$, as expected (see Fig. 4). In these implementations, the variable control was implemented as piecewise constant within each cell, requiring source terms resulting from the discontinuities at cell boundaries and making multidimensional implementations complex.[82,128] This complexity can be alleviated by a formulation using a continuously variable control, which, as shown in Section 6.3, results in a volumetric source term that can be implemented relatively straightforwardly. Such a formulation will require the development of a method for (approximately) describing the local temperature variation as recovered from cell-based sampling using functions with continuous derivatives.

A hybrid approach for reducing the computational cost associated with deterministic discretization-based solution of the Boltzmann equation in the relaxation-time approximation has recently been proposed by Loy et al.[144] In this approach, the computational cost is reduced by identifying a cutoff lengthscale below which transport is expected to be diffusive and using the heat conduction equation to treat modes with shorter expected travel distances between scattering events. The computational speedup results from reducing the number of modes for which the BTE needs to be solved (solving the heat conduction equation for the remaining modes is significantly more efficient since no angular discretization is required), but also because the remaining modes are the ones that are typically less costly to treat by the BTE.[144] Although this approach is, in general, approximate, the small coupling between different modes in the relaxation-time approximation means that if this cutoff length scale is chosen conservatively (that is the Knudsen number based on it is small), then the error is small (on the order of a few percent). The resulting speedup is on the order of 100. As in the case of the linearized method of Section 6, it is not clear whether or not this approach can be successfully extended to more realistic scattering models that feature considerably more complex coupling between different modes.

8. DISCUSSION

As in many fields involving transport mediated by particles, MC methods are one of the prevalent computational methods because they combine simplicity with computational efficiency while retaining an intuitive connection to the problem physics. Review of the literature suggests that, similarly to the rarefied-gas-dynamics field,[145] MC methods currently hold a computational advantage over discretization-based methods of solution for problems of engineering interest, where an accuracy of the order of 1% is sufficient. This appears to be in part because of the good balance—in the context of current computational resources—they strike between statistical uncertainty and efficiency. In contrast to deterministic methods which exhibit no statistical uncertainty but need to discretize the complete phase space, MC methods avoid some of the discretization, thus making simulations more feasible, by introducing statistical uncertainty. Paradoxically, the resulting robustness has its origins in the poor convergence of statistical sampling with the number of samples: the “flip-side” of the square-root-convergence is that the solution quality does not degrade fast with decreasing number of samples (a simulation with 10 times less samples, will exhibit a statistical uncertainty that is only 3 times larger). As a result, state of the art MC methods are able to provide well-resolved solutions to three-dimensional, transient problems in realistic geometries without using massively parallel computational resources.

At the same time, using similar computational resources and no additional simplifying assumptions (e.g., gray approximation), state of the art discretization-based methods of solution are currently limited to moderately resolved two-dimensional problems.[144–146]

It is not yet clear what the effect of the trend towards increasingly larger numbers of cores per chip will be on this balance. On one hand, more cores seems to favor MC methods which lend themselves naturally to parallel implementation via ensemble averaging. On the other hand, the slow statistical convergence of MC sampling means that as the available computational resources increase (either via faster processors or better parallel efficiencies), MC methods are expected to benefit less compared to high-order discretization-based schemes. MC methods can remain competitive for a long time via variance reduction techniques such as the ones discussed in Section 4, which significantly reduce the level of statistical uncertainty.

Although having their origin in the DSMC method, phonon MC simulation methods have not been subject to the same level of numerical analysis, perhaps because they are significantly more recent than DSMC (the convergence proof for DSMC[4] arrived almost 30 years after Bird's original paper). Although it is expected that many of the results derived for DSMC discussed in Section 2.6, at least qualitatively, hold for phonon MC, rigorous numerical analysis of the latter is still warranted, especially for the collision (scattering) part of the algorithm which is fairly different to those of dilute gases and in some implementations quite ad-hoc. The benefits will include improved understanding of the approximations involved, but also possibly reduced numerical error; for example, for certain classes of scattering operators, simulation of the scattering process with no time step error is possible[64,98] (note that this does not eliminate the splitting error, which in the first example is absent, but in the second is not).

Deviational methods have been subject to considerably less analysis. For example, little is known about their fluctuation spectrum and the latter's relation to the nonequilibrium fluctuation spectrum associated with phonon transport. Expressions analogous to Eq. (60), relating the statistical uncertainty as a function of the number of computational (deviational) particles, would be very useful because they would allow users to select simulation parameters such as N_{eff} and $\mathcal{E}_{\text{eff}}$ without trial and error.

Recent interest has focused on low-dimensional materials in which transport is affected by a number of features that cannot be accurately captured by the relaxation-time approximation.[30,112,113] The recently developed[46–48] deviational formulation for integrating the BTE with the more realistic scattering operator (10) is an exciting first step towards high-fidelity solutions of complex problems of engineering interest involving phonon transport. As discussed in Refs. 46–48, considerable improvements to this first step are possible using ideas reviewed here, such kinetic-Monte-Carlo-type algorithms in which computational particles evolve independently, steady-state formulations and methods for efficiently terminating trajectories. A more complete discussion can be found in Ref. 46.

ACKNOWLEDGMENTS

This work was supported in part by the Singapore-MIT Alliance program. J.-P. M. Péraud additionally acknowledges financial support from Ecole National des Ponts et Chaussées

and the MIT Department of Materials Science and Engineering through a Graduate Fellowship. C. D. Landon additionally acknowledges financial support from the National Science Foundation Graduate Research Fellowship Program.

REFERENCES

1. Hammersley, J. M. and Handscomb, D. C., *Monte Carlo Methods*, Wiley, Hoboken, 1964.
2. Metropolis, N., Rosenbluth, A. W., Rosenbluth, M. N., Teller, A. H., and Teller, E., Equation of State Calculations by Fast Computing Machines, *J. Chem. Phys.*, vol. 21, pp. 1087–1092, 1953.
3. Panagiotopoulos, A. Z., Direct Determination of Phase Coexistence Properties of Fluids by Monte Carlo Simulation in a New Ensemble, *Mol. Phys.*, vol. 61, pp. 813–826, 1987.
4. Wagner, W., A Convergence Proof for Bird's Direct Simulation Monte Carlo Method for the Boltzmann Equation, *J. Stat. Phys.*, vol. 66, pp. 1011–1044, 1992.
5. Wagner, W., Deviational Particle Monte Carlo for the Boltzmann Equation, *Monte Carlo Methods Appl.*, vol. 14, pp. 191–268, 2008.
6. Bird, G. A., Approach to Translational Equilibrium in a Rigid Sphere Gas, *Phys. Fluids*, vol. 6, pp. 1518–1520, 1963.
7. Hadjiconstantinou, N. G., Garcia, A. L., Bazant, M. Z., and He, G., Statistical Error in Particle Simulations of Hydrodynamic Phenomena, *J. Comput. Phys.*, vol. 187, pp. 274–297, 2003.
8. Hadjiconstantinou, N. G., The Limits of Navier-Stokes Theory and Kinetic Extensions for Describing Small Scale Gaseous Hydrodynamics, *Phys. Fluids*, vol. 18, p. 111301, 2006.
9. Vincenti, W. G. and Kruger, C. H., *Introduction to Physical Gas Dynamics*, Wiley, Hoboken, 1965.
10. Bird, G. A., *Molecular Gas Dynamics and the Direct Simulation of Gas Flows*, Clarendon Press, Oxford, UK, 1994.
11. Cercignani, C., *The Boltzmann Equation and Its Applications*, Springer-Verlag, New York, 1988.
12. Al-Mohssen, H. A. and Hadjiconstantinou, N. G., Arbitrary-Pressure Chemical Vapor Deposition Modeling Using Direct Simulation Monte Carlo with Nonlinear Surface Chemistry, *J. Comput. Phys.*, vol. 198, pp. 617–627, 2004.
13. Gallis, M. A., Rader, D. J., and Torczynski, J. R., Calculations of the Near-Wall Thermophoretic Force in Rarefied Gas Flow, *Phys. Fluids*, vol. 14, pp. 4290–4301, 2002.
14. Alexander, F. J., Garcia, A. L., and Alder, B. J., Direct Simulation Monte Carlo for Thin-Film Bearings, *Phys. Fluids*, vol. 6, pp. 3854–3860, 1994.
15. Gallis, M. A. and Torczynski, J. R., An Improved Reynolds-Equation Model for Gas Damping of Microbeam Motion, *J. Microelectromech. Syst.*, vol. 13, pp. 653–659, 2004.
16. Takata, S., Sugimoto, H., and Kosuge, S., Gas Separation by Means of the Knudsen Compressor, *Eur. J. Mech. B*, vol. 26, pp. 155–181, 2007.
17. Hadjiconstantinou, N. G. and Simek, O., Constant-Wall-Temperature Nusselt Number in Micro and Nano Channels, *ASME J. Heat Transfer*, vol. 124, pp. 356–364, 2002.
18. Hadjiconstantinou, N. G., Dissipation in Small Scale Gaseous Flows, *ASME J. Heat Transfer*, vol. 125, pp. 944–947, 2003.

19. Shi, L., Thermal Transport Measurement Techniques for Nanowires and Nanotubes, *Ann. Rev. Heat Transfer*, vol. 16, pp. 101–134, 2013.

20. Klitsner, T., VanCleve, J. E., Fisher, H. E., and Pohl, R. O., Phonon Radiative Heat Transfer and Surface Scattering, *Phys. Rev. B*, vol. 38, pp. 7576–7594, 1988.

21. Lacroix, D., Joulain, K., Terris, D., and Lemonnier, D., Monte Carlo Modeling of Phonon Transport in Nanodevices, *J. Phys. Conf. Ser.*, vol. 92, pp. 1–4, 2007.

22. Moore, A. L., Saha, S. K., Prasher, R. S., and Shi, L., Phonon Backscattering and Thermal Conductivity Suppression in Sawtooth Nanowires, *Appl. Phys. Lett.*, vol. 93, p. 083112, 2008.

23. Roberts, N. A. and Walker, D. G., Computational Study of Thermal Rectification from Nanostructured Interfaces, *ASME J. Heat Transfer*, vol. 133, p. 092401, 2011.

24. Jeng, M. S., Yang, R., Song, D., and Chen, G., Modeling the Thermal Conductivity and Phonon Transport in Nanoparticle Composites Using Monte Carlo Simulation, *ASME J. Heat Transfer*, vol. 130, p. 042410, 2008.

25. Huang, M.-J. and Chuang, P.-Y., An Investigation into the Lattice Thermal Conductivity of Random Nanowire Composites, *Int. J. Heat Mass Transfer*, vol. 55, pp. 3704–3712, 2012.

26. Randrianalisoa, J. and Baillis, D., Monte Carlo Simulation of Cross-Plane Thermal Conductivity of Nanostructured Porous Silicon Films, *J. Appl. Phys.*, vol. 103, p. 053502, 2008.

27. Chen, G., *Nanoscale Energy Transport and Conversion*, Oxford University Press, New York, 2005.

28. Hao, Q., Chen, G., and Jeng, M. S., Frequency-Dependent Monte Carlo Simulation of Phonon Transport in Two-Dimensional Porous Silicon with Aligned Pores, *J. Appl. Phys.*, vol. 106, p. 114321, 2009.

29. Tian, W. and Yang, R., Thermal Conductivity Modeling of Compacted Nanowire Composites, *J. Appl. Phys.*, vol. 101, p. 054320, 2007.

30. Seol, J. H., Jo, I., Moore, A. L., Lindsay, L., Aitken, Z. H., Pettes, M. T., Li, X., Yao, Z., Huang, R., Broido, D., Mingo, N., Ruoff, R. S., and Shi, L., Two-Dimensional Phonon Transport in Supported Graphene, *Science*, vol. 328, pp. 213–216, 2010.

31. Lindsay, L., Broido, D. A., and Mingo, N., Flexural Phonons and Thermal Transport in Graphene, *Phys. Rev. B*, vol. 82, p. 115427, 2010.

32. Balandin, A. A., Thermal Properties of Graphene and Nanostructured Carbon Materials, *Nat. Mater.*, vol. 10, pp. 569–581, 2011.

33. Pop, E., Dutton, R. W., and Goodson, K. E., Analytic Band Monte Carlo Model for Electron Transport in Si Including Acoustic and Optical Phonon Dispersion, *J. Appl. Phys.*, vol. 96, p. 4998, 2004.

34. Walker, D. G. and Weller, R. A., Phonon Production and Nonequilibrium Transport from Ion Strikes, *IEEE Trans. Nucl. Sci.*, vol. 51, pp. 3318–3321, 2004.

35. Wong, B. T. and Mengüc, M. P., A Unified Monte Carlo Treatment of the Transport of Electromagnetic Energy, Electrons, and Phonons in Absorbing and Scattering Media, *J. Quant. Spectros. Radiat. Transfer*, vol. 111, pp. 399–419, 2010.

36. Wong, B. T., Francoeur, M., and Mengüc, M. P., A Monte Carlo Simulation for Phonon Transport within Silicon Structures at Nanoscales with Heat Generation, *Int. J. Heat Mass Transfer*, vol. 54, pp. 1825–1838, 2011.

37. Ramayya, E. B., Maurer, L. N., Davoody, A. H., and Knezevic, I., Thermoelectric Properties

of Ultrathin Silicon Nanowires, *Phys. Rev. B*, vol. 86, p. 115328, 2012.

38. Pop, E., Monte Carlo Transport and Heat Generation in Semiconductors, *Ann. Rev. Heat Transfer*, vol. 17, pp. 385–423, 2014.
39. Minnich, A. J., Chen, G., Mansoor, S., and Yilbas, B. S., Quasiballistic Heat Transfer Studied Using the Frequency-Dependent Boltzmann Transport Equation, *Phys. Rev. B*, vol. 84, p. 235207, 2011.
40. Minnich, A. J., Determining Phonon Mean Free Paths from Observation of Quasiballistic Thermal Transport, *Phys. Rev. Lett.*, vol. 109, p. 205901, 2012.
41. Minnich, A. J., Measuring Phonon Mean Free Paths Using Thermal Conductivity Spectroscopy, *Ann. Rev. Heat Transfer*, vol. 16, pp. 183–210, 2013.
42. Piekos, E. S., Graham, S., and Wong, C. C., Multiscale Thermal Transport, Technical Report SAND2004-0531, Sandia National Laboratories, Albuquerque, 2004.
43. Chen, G., Size and Interface Effects on Thermal Conductivity of Superlattices and Periodic Thin-Film Structures, *J. Heat Transfer*, vol. 119, pp. 220–229, 1997.
44. Schelling, P. K. and Phillpot, S. R., Multiscale Simulation of Phonon Transport in Superlattices, *J. Appl. Phys.*, vol. 93, pp. 5377–5387, 2003.
45. Landon, C. D. and Hadjiconstantinou, N. G., Low-Variance Monte Carlo Simulation of Thermal Transport in Graphene, *International Mechanical Engineering Congress and Exposition*, Paper No. IMECE2012-87957, 2012.
46. Landon, C. D., A Deviational Monte Carlo Formulation of Ab Initio Phonon Transport and its Application to the Study of Kinetic Effects in Graphene Ribbons, PhD Thesis, Massachusetts Institute of Technology, Cambridge, MA, 2014.
47. Landon, C. D. and Hadjiconstantinou, N. G., Simulation of Heat Transport in Graphene Nanoribbons Using the Ab-Initio Scattering Operator, in *International Mechanical Engineering Congress and Exposition*, Paper No. IMECE2014-36473, 2014.
48. Péraud, J.-P. M., Landon, C. D., and Hadjiconstantinou, N. G., Deviational Methods for Small-Scale Phonon Transport, *Mech. Eng. Rev.*, vol. 1, no. 2, p. 14-00243, 2014.
49. Ecsedy, D. J. and Klemens, P. G., Thermal Resistivity of Dielectric Crystals Due to Four-Phonon Processes and Optical Modes, *Phys. Rev. B*, vol. 15, pp. 5957–5962, 1976.
50. Srivastava, G. P., *The Physics of Phonons*, Taylor & Francis Group, New York, 1990.
51. Pascual-Gutiérrez, J. A., Murthy, J. Y., and Viskanta, R., Thermal Conductivity and Phonon Transport Properties of Silicon Using Perturbation Theory and the Environment-Dependent Interatomic Potential, *J. Appl. Phys.*, vol. 106, p. 063532, 2009.
52. Ziman, J. M., *Electrons and Phonons*, Clarendon Press, Oxford, UK, 1960.
53. Murthy, J. Y., Review of Multiscale Simulation in Sub Micron Heat Transfer, *Int. J. Multiscale Comput. Eng.*, vol. 3, pp. 5–31, 2005.
54. Srivastava, G. P., Theories of Phonon Transport in Bulk and Nanostructured Solids, *Topics Appl. Phys.*, vol. 128, pp. 81–114, 2014.
55. Bhatnagar, P. L., Gross, E. P., and Krook, M., A Model for Collision Processes in Gases, I. Small Amplitude Processes in Charged and Neutral One-Component Systems, *Phys. Rev.*, vol. 94, pp. 511–525, 1954.
56. Andries, P., Tallec, P. L., Perlat, J.-P., and Perthame, B., The Gaussian-BGK Model of Boltz-

mann Equation with Small Prandtl Number, *Eur. J. Mech. B*, vol. 19, pp. 813–830, 2000.

57. Callaway, J., Model for Lattice Thermal Conductivity at Low Temperatures, *Phys. Rev.*, vol. 113, pp. 1046–1051, 1959.
58. Holland, M. G., Analysis of Lattice Thermal Conductivity, *Phys. Rev.*, vol. 95, pp. 2461–2471, 1963.
59. Chapman, S. and Cowling, T. G., *The Mathematical Theory of Non-Uniform Gases*, Cambridge University Press, Cambridge, UK, 1991.
60. Turney, J. E., McGaughey, A. J. H., and Amon, C. H., In-Plane Phonon Transport in Thin Films, *J. Appl. Phys.*, vol. 107, p. 024317, 2009.
61. Péraud, J.-P. M. and Hadjiconstantinou, N. G., Efficient Simulation of Multidimensional Phonon Transport Using Energy-Based Variance-Reduced Monte Carlo Formulations, *Phys. Rev. B*, vol. 84, p. 205331, 2011.
62. Majumdar, A., Microscale Heat Conduction in Dielectric Thin Films, *J. Heat Transfer*, vol. 115, pp. 7–16, 1993.
63. Cercignani, C., *Slow Rarefied Flows*, Birkhäuser Verlag, Basel, 2006.
64. Péraud, J.-P. M. and Hadjiconstantinou, N. G., An Alternative Approach to Efficient Simulation of Micro/Nanoscale Phonon Transport, *Appl. Phys. Lett.*, vol. 101, p. 153114, 2012.
65. Sone, Y., *Molecular Gas Dynamics: Theory, Techniques, and Applications*, Birkhäuser, Boston, 2007.
66. Aoki, K., Takata, S., and Golse, F., A Rarefied Gas Flow Caused by a Discontinuous Wall Temperature, *Phys. Fluids*, vol. 13, pp. 2645–2661, 2001.
67. Homolle, T. M. M. and Hadjiconstantinou, N. G., A Low-Variance Deviational Simulation Monte Carlo for the Boltzmann Equation, *J. Comput. Phys.*, vol. 226, pp. 2341–2358, 2007.
68. Strang, G., On the Construction and Comparison of Difference Schemes, *SIAM J. Numer. Anal.*, vol. 5, pp. 506–517, 1968.
69. Alexander, F. J. and Garcia, A. L., The Direct Simulation Monte Carlo Method, *Comput. Phys.*, vol. 11, pp. 588–593, 1997.
70. Alexander, F. J., Garcia, A. L., and Alder, B. J., Cell Size Dependence of Transport Coefficients in Stochastic Particle Algorithms, *Phys. Fluids*, vol. 10, pp. 1540–1542, 1998.
71. Hadjiconstantinou, N. G., Analysis of Discretization in the Direct Simulation Monte Carlo, *Phys. Fluids*, vol. 12, pp. 2634–2638, 2000.
72. Alexander, F. J., Garcia, A. L., and Alder, B. J., Erratum: Cell Size Dependence of Transport Coefficients in Stochastic Particle Algorithms (*Phys. Fluids*, vol. 10, p. 1540, 1998), *Phys. Fluids*, vol. 12, p. 731, 2000.
73. Garcia, A. L. and Wagner, W., Timestep Truncation Error in Direct Simulation Monte Carlo, *Phys. Fluids*, vol. 12, pp. 2621–2633, 2000.
74. Rader, D. J., Gallis, M. A., Torczynski, J. R., and Wagner, W., Direct Simulation Monte Carlo Convergence Behavior of the Hard-Sphere Gas Thermal Conductivity for Fourier Heat Flow, *Phys. Fluids*, vol. 18, p. 077102, 2006.
75. Gallis, M. A., Torczynski, J. R., Rader, D. J., Tij, M., and Santos, A., Normal Solutions of the Boltzmann Equation for Highly Nonequilibrium Fourier Flow and Couette Flow, *Phys. Fluids*, vol. 18, p. 017104, 2006.

76. Peterson, R. B., Direct Simulation of Phonon-Mediated Heat-Transfer in a Debye Crystal, *J. Heat Transfer*, vol. 118, pp. 815–822, 1994.

77. Mazumder, S. and Majumdar, A., Monte Carlo Study of Phonon Transport in Solid Thin Films Including Dispersion and Polarization, *J. Heat Transfer*, vol. 123, pp. 749–759, 2001.

78. Narumanchi, S. V. J., Murthy, J. Y., and Amon, C. H., Submicron Heat Transport Model in Silicon Accounting for Phonon Dispersion and Polarization, *J. Heat Transfer*, vol. 126, pp. 946–955, 2004.

79. Lacroix, D., Joulain, K., and Lemonnier, D., Monte Carlo Transient Phonon Transport in Silicon and Germanium at Nanoscales, *Phys. Rev. B*, vol. 72, p. 064305, 2005.

80. Rjasanow, S. and Wagner, W., *Stochastic Numerics for the Boltzmann Equation*, Springer-Verlag, Berlin, 2005.

81. Press, W., Teukolsky, S. A., Vetterling, W. T., and Flannery, B. P., *Numerical Recipes in C*, Cambridge University Press, Cambridge, UK, 1992.

82. Radtke, G. A. and Hadjiconstantinou, N. G., Variance-Reduced Particle Simulation of the Boltzmann Transport Equation in the Relaxation-Time Approximation, *Phys. Rev. E*, vol. 79, p. 056711, 2009.

83. Soffer, S. B., Statistical Model of the Size Effect in Electrical Conduction, *J. Appl. Phys.*, vol. 38, pp. 1710–1716, 1967.

84. Aksamija, Z. and Knezevic, I., Anisotropy and Boundary Scattering in the Lattice Thermal Conductivity of Silicon Nanomembranes, *Phys. Rev. B*, vol. 82, p. 045319, 2010.

85. Volz, S. and Chen, G., Molecular Dynamics Simulation of Thermal Conductivity of Silicon Nanowires, *Appl. Phys. Lett.*, vol. 75, pp. 2056–2059, 1999.

86. Mital, A. and Mazumder, S., Monte Carlo Study of Phonon Heat Conduction in Silicon Thin Films Including Contributions of Optical Phonons, *J. Heat Transfer*, vol. 132, p. 052402, 2010.

87. Terris, D., Joulain, K., Lemonnier, D., and Lacroix, D., Modeling Semiconductor Nanostructures Thermal Properties: The Dispersion Role, *J. Appl. Phys.*, vol. 105, p. 073516, 2009.

88. Chalopin, Y., Esfarjani, K., Henry, A., Volz, S., and Chen, G., Thermal Interface Conductance in Si/Ge Superlattices by Equilibrium Molecular Dynamics, *Phys. Rev. B*, vol. 85, p. 195302, 2012.

89. Chalopin, Y., Rajabpour, A., Han, H., Ni, Y., and Volz, S., Equilibrium Molecular Dynamics Simulations on Interfacial Phonon Transport, *Ann. Rev. Heat Transfer*, vol. 17, pp. 147–176, 2014.

90. Sadasivam, S., Che, Y., Huang, Z., Chen, L., Kumar, S., and Fisher, T. S., The Atomistic Green's Function Method for Interfacial Phonon Transport, *Ann. Rev. Heat Transfer*, vol. 17, pp. 89–145, 2014.

91. Stoner, R. J. and Maris, H. J., Kapitza Conductance and Heat Flow between Solids at Temperature from 50 to 300 K, *Phys. Rev. B*, vol. 48, pp. 16373–16387, 1993.

92. Hopkins, P. E., Multiple Phonon Processes Contributing to Inelastic Scattering During Thermal Boundary Conductance at Solid Interfaces, *J. Appl. Phys.*, vol. 106, p. 013528, 2009.

93. Duda, J. C., Hopkins, P. E., Smoyer, J. L., Bauer, M. L., English, T. S., Satonstall, C. B., and Norris, P. M., On the Assumption of Detailed Balance in Prediction of Diffusive Transmission Probability During Interfacial Transport, *Nano Microscale Thermophys. Eng.*, vol. 14, pp. 21–

33, 2010.

94. Chen, Y., Li, D., Lukes, J. R., and Ni, Z., Monte Carlo Simulation of Silicon Nanowire Thermal Conductivity, *J. Heat Transfer*, vol. 127, pp. 1129–1137, 2005.
95. Randrianalisoa, J. and Baillis, D., Monte Carlo Simulation of Cross-Plane Thermal Conductivity of Nanostructured Porous Silicon Films, *J. Heat Transfer*, vol. 130, p. 072404, 2008.
96. Henry, A. S. and Chen, G., Spectral Phonon Transport Properties of Silicon Based on Molecular Dynamics Simulations and Lattice Dynamics, *J. Comput. Theoret. Nanosci.*, vol. 5, pp. 141–152, 2008.
97. Minnich, A. J., *Exploring Electron and Phonon Transport at the Nanoscale for Thermoelectric Energy Conversion*, PhD Thesis, Massachusetts Institute of Technology, Cambridge, MA, 2011.
98. Radtke, G. A., Hadjiconstantinou, N. G., and Wagner, W., Low-Noise Monte Carlo Simulation of the Variable Hard-Sphere Gas, *Phys. Fluids*, vol. 23, p. 030606, 2011.
99. Tian, Z., Lee, S., and Chen, G., A Comprehensive Review of Heat Transfer in Thermoelectric Material and Devices, *Ann. Rev. Heat Transfer*, vol. 17, pp. 425–483, 2014.
100. Taguchi, S. and Charrier, P., Rarefied Gas Flow Oven an In-Line Array of Circular Cylinders, *Phys. Fluids*, vol. 20, p. 067103, 2008.
101. Taguchi, S., Diffusion Model for Knudsen-Type Compressor Composed of Period Arrays of Circular Cylinders, *Phys. Fluids*, vol. 22, p. 102001, 2010.
102. Omini, M. and Sparavigna, A., An Alternative Approach to the Phonon Boltzmann Equation in the Theory of Thermal Conductivity, *Phys. B*, vol. 212, pp. 101–112, 1995.
103. Fugallo, G., Lazzeri, M., Paulatto, L., and Mauri, F., Ab Initio Variational Approach for Evaluating Lattice Thermal Conductivity, *Phys. Rev. B*, vol. 88, p. 045430, 2013.
104. Mingo, N., Steward, D., Broido, D., Lindsay, L., and Li, W., Ab Initio Thermal Transport, *Topics Appl. Phys.*, vol. 128, pp. 137–173, 2014.
105. McGaughey, A. J. H. and Larkin, J. M., Predicting Phonon Properties from Equilibrium Molecular Dynamics Simulations, *Ann. Rev. Heat Transfer*, vol. 17, pp. 49–87, 2014.
106. Esfarjani, K., Chen, G., and Stokes, H. T., Heat Transport in Silicon from First-Principles Calculations, *Phys. Rev. B*, vol. 84, p. 085204, 2011.
107. Esfarjani, K., Garg, J., and Chen, G., Modeling Heat Conduction from First-Principles, *Ann. Rev. Heat Transfer*, vol. 17, pp. 9–47, 2014.
108. Shiomi, J., Nonequilibrium Molecular Dynamics Methods for Lattice Heat Conduction Calculations, *Ann. Rev. Heat Transfer*, vol. 17, pp. 177–203, 2014.
109. McGaughey, A. J. H. and Kaviany, M., Quantitative Validation of the Boltzmann Transport Equation Phonon Thermal Conductivity Model under the Single-Mode Relaxation Time Approximation, *Phys. Rev. B*, vol. 69, p. 094303, 2004.
110. Turney, J. E., Landry, E. S., McGaughey, A. J. H., and Amon, C. H., Predicting Phonon Properties and Thermal Conductivity from Anharmonic Lattice Dynamics Calculations and Molecular Dynamics Simulations, *Phys. Rev. B*, vol. 79, p. 064301, 2009.
111. McGaughey, A. J. H. and Kaviany, M., Erratum: Quantitative Validation of the Boltzmann Transport Equation Phonon Thermal Conductivity Model under the Single-Mode Relaxation Time Approximation (*Phys. Rev. B*, vol. 69, p. 094303, 2004), *Phys. Rev. B*, vol. 79, p. 189901, 2009.

112. Singh, D., Murthy, J. Y., and Fisher, T. S., Spectral Phonon Conduction and Dominant Scattering Pathways in Graphene, *J. Appl. Phys.*, vol. 110, p. 094312, 2011.

113. Singh, D., Murthy, J. Y., and Fisher, T. S., On the Accuracy of Classical and Long Wavelength Approximation for Phonon Transport in Graphene, *J. Appl. Phys.*, vol. 110, p. 113510, 2011.

114. Matsumoto, M., Xiao, P., and Kunisawa, T., Relaxation of Phonons in Classical MD Simulations, In *Proceedings of 2007 ASME-JSME Thermal Engineering Summer Heat Transfer Conference*, Vancouver, Canada, 2007.

115. Cahill, D. G., Ford, W. K., Goodson, K. E., Mahan, G. D., Majumdar, A., Maris, H. J., Merlin, R., and Phillpot, S. R., Nanoscale Thermal Transport, *J. Appl. Phys.*, vol. 93, pp. 793–818, 2003.

116. Sinha, S. and Goodson, K. E., Review: Multiscale Thermal Modeling for Nanoelectronics, *Int. J. Multiscale Comput. Eng.*, vol. 3, pp. 107–133, 2005.

117. Garcia, A. L. and Wagner, W., Direct Simulation Monte Carlo Method for the Uehling-Uhlenbeck-Boltzmann Equation, *Phys. Rev. E*, vol. 68, p. 056703, 2003.

118. Masao, Y., Okano, M., and Matsumoto, M., DSMC Scheme to Study Phonon Dynamics, *J. Mech. Sci. Technol.*, vol. 25, pp. 21–26, 2011.

119. Matsumoto, M., Okano, M., and Masao, Y., DSMC Scheme for Phonon Transport in Solid Thin Films, *J. Heat Transfer*, vol. 134, p. 051009, 2012.

120. Cahill, D., Goodson, K. E., and Majumdar, A., Thermometry and Thermal Transport in Micro/Nanoscale Solid-State Devices and Structures, *J. Heat Transfer*, vol. 124, pp. 223–240, 2002.

121. Cahill, D. G., Analysis of Heat Flow in Layered Structures for Time-Domain Thermoreflectance, *Rev. Scient. Instruments*, vol. 75, pp. 5119–5122, 2004.

122. Schmidt, A. J., Chen, X., and Chen, G., Pulse Accumulation, Radial Heat Conduction, and Anisotropic Thermal Conductivity in Pump-Probe Transient Thermoreflectance, *Rev. Scient. Instruments*, vol. 79, p. 114902, 2008.

123. Schmidt, A., Pump Probe Thermoreflectance, *Ann. Rev. Heat Transfer*, vol. 16, pp. 159–181, 2013.

124. Zeng, L., Experimental and Numerical Investigation of Phonon Mean Free Path Distribution, Master's Thesis, Massachusetts Institute of Technology, Cambridge, MA, 2013.

125. Baker, L. L. and Hadjiconstantinou, N. G., Variance Reduction for Monte Carlo Solutions of the Boltzmann Equation, *Phys. Fluids*, vol. 17, p. 051703, 2005.

126. Spanier, J. and Gelbard, E. M., *Monte Carlo Principles and Neutron Transport Problems*, Addison-Wesley, Reading, MA, 1969.

127. Case, K. M. and Zweifel, P. F., *Linear Transport Theory*, Addison-Wesley, Reading, MA, 1967.

128. Radtke, G. A., Péraud, J.-P. M., and Hadjiconstantinou, N. G., On Efficient Simulations of Multiscale Kinetic Transport, *Philos. Trans. R. Soc. A*, vol. 371, p. 20120182, 2013.

129. Irving, D. C., The Adjoint Boltzmann Equation and its Simulation by Monte Carlo, *Nucl. Eng. Design*, vol. 15, pp. 273–292, 1971.

130. Voter, A. F., *Introduction to the Kinetic Monte Carlo Method*, Vol. 235 of NATO Science Series, Springer, 2007.

131. Péraud, J.-P. M. and Hadjiconstantinou, N. G., Deviational Phonons and Thermal Transport

at the Nanoscale, *The 2012 International Mechanical Engineering Congress and Exposition*, Paper No. IMECE2012-87547, ASME, New York, 2012.

132. Pareschi, L. and Russo, G., Asymptotic Preserving Monte Carlo Methods for the Boltzmann Equation, *Transport Theory Statist. Phys.*, vol. 29, pp. 415–430, 2000.
133. Wennberg, B., Trazzi, S., and Pareschi, L., Adaptive and Recursive Time Relaxed Monte Carlo Methods for Rarefied Gas Dynamics, *J. Scient. Comput.*, vol. 31, pp. 1379–1398, 2009.
134. Modest, M. F., Backward Monte Carlo Simulations in Radiative Heat Transfer, *J. Heat Transfer*, vol. 125, pp. 58–62, 2003.
135. Péraud, J.-P. M., PhD Thesis, Massachusetts Institute of Technology, Cambridge, MA, in progress.
136. Wadsworth, D. C. and Erwin, D. A., One-Dimensional Hybrid Continuum/Particle Simulation Approach for Rarefied Hypersonic Flows, AIAA Paper No. 90-1690, 1990.
137. Hadjiconstantinou, N. G., Hybrid Atomistic-Continuum Formulations and the Moving Contact-Line Problem, *J. Computat. Phys.*, vol. 154, pp. 245–265, 1999.
138. Hadjiconstantinou, N. G., Discussion of Recent Developments in Hybrid Atomistic-Continuum Methods for Multiscale Hydrodynamics, *Bull. Polish Acad. Sci. Micro Nanoscale Mech.*, vol. 53, pp. 335–342, 2005.
139. Garcia, A. L., Bell, J. B., Crutchfield, W. Y., and Alder, B. J., Adaptive Mesh and Algorithm Refinement Using Direct Simulation Monte Carlo, *J. Computat. Phys.*, vol. 154, pp. 134–155, 1999.
140. Wijesinghe, H. S., Hornung, R., Garcia, A. L., and Hadjiconstantinou, N. G., Three-Dimensional Hybrid Continuum-Atomistic Simulations for Multiscale Hydrodynamics, *J. Fluids Eng.*, vol. 126, 2004.
141. Schwartzentruber, T. E. and Boyd, I. D., A Modular Particle-Continuum Numerical Method for Hypersonic Non-Equilibrium Gas Flows, *J. Computat. Phys.*, vol. 225, pp. 1159–1174, 2007.
142. Degond, P., Dimarco, G., and Mieussens, L., A Multiscale Kinetic-Fluid Solver with Dynamic Localization of Kinetic Effects, *J. Computat. Phys.*, vol. 229, pp. 4907–4933, 2007.
143. Wang, W. and Boyd, I. D., Predicting Continuum Breakdown in Hypersonic Viscous Flows, *Phys. Fluids*, vol. 15, pp. 91–100, 2003.
144. Loy, J. M., Murthy, J. Y., and Singh, D., A Fast Hybrid Fourier-Boltzmann Transport Equation Solver for Nongray Phonon Transport, *J. Heat Transfer*, vol. 135, p. 011008, 2013.
145. Baker, L. L. and Hadjiconstantinou, N. G., Variance-Reduced Monte Carlo Solutions of the Boltzmann Equation for Low-Speed Gas Flows: A Discontinuous Galerkin Formulation, *Int. J. Numer. Methods Fluids*, vol. 58, pp. 381–402, 2008.
146. Romano, G. and Grossman, J. C., Mesoscale Modeling of Phononic Thermal Conductivity of Porous Si: Interplay between Porosity, Morphology and Surface Roughness, *J. Computat. Electr.*, vol. 11, pp. 8–13, 2012.
147. Hamzeh, H. and Aniel, F., Monte Carlo Study of Phonon Dynamics in III-V Compounds, *J. Appl. Phys.*, vol. 109, p. 063511, 2011.